NUMERICAL SIMULATION OF FREE STANDING HYBRID RISERS

A Thesis

by

TIANCONG HOU

Submitted to the Office of Graduate and Professional Studies of
Texas A&M University
in partial fulfillment of the requirements for the degree of

MASTER OF SCIENCE

Chair of Committee,	Jun Zhang
Committee Members,	Richard Mercier
	Guy Battle
Head of Department,	Robin Autenrieth

August 2014

Major Subject: Ocean Engineering

ABSTRACT

Free Standing Hybrid Riser (FSHR) is an innovative concept for the riser to transport oil and gas from the seabed to a floating production platform deployed in deep water. A FSHR mainly consists of a buoyancy can, a vertical steel riser, a flexible jumper and an upper riser assembly (URA). This study focusses on the development of the numerical scheme for the dynamic simulation of a FSHR whose flexible jumper is connected to a moored floating production vessel, say floating production, storage and offloading (FPSO). The numerical scheme is mainly based on an existing in-house numerical code, known as COUPLE. In using COUPLE, URA is modeled as a rigid body. The URA connects a vertical steel riser and a flexible jumper, both of which are modeled by beam elements (experienced both tensions and bending moments) in COUPLE. The buoyancy can is connected to the URA through a tether chain, which provides the vertical upright force on the URA and in turn the tension to the vertical riser. The tether chain is modeled by bar elements (experienced only tensions) while the buoyancy can is modeled as a rigid cylinder (beam element). The motions and forces of the two rigid bodies, namely URA and the buoyancy can, are coupled in the simulation. Because the connection between the URA and steel riser is considered as „rigid", an accurate numerical scheme modeling a rotational spring connecting the URA and steel riser is developed for calculating the bending moment applied at the upper end of the riser. Given the motion at the upper end of the flexible jumper (connecting to a FPSO), numerical simulations are made for two different FSHRs. The results simulated using

COUPLE are in satisfactory agreement with those obtained using OrcaFlex, a commercial code widely used by the offshore industry. Furthermore, the vortex induced motion (VIM) of the buoyancy can is considered in the simulation and its effects on the motion of the FSHR are explored, which is compared with the corresponding model tests. The ability to simulate the dynamics of FSHRs developed in this study may be helpful for the future design of FSHRs.

ACKNOWLEDGEMENTS

I would like thank my committee chair, Prof. Jun Zhang, for his guidance and kindly support throughout my research. I would as well like to thank my committee members, Prof. Richard Mercier and Prof. Guy Battle for their help during my research. I would also like to express my thanks to Dr. Gwo-ang Chang who provided useful data.

Finally, thanks to my parents for their encouragement and support throughout the duration of my studies in the United States.

TABLE OF CONTENTS

Page

LIST OF FIGURES

Page

LIST OF TABLES

Page

1. INTRODUCTION

1.1 Background and Significance

A riser system is essentially a pipe connecting a floater at the water surface and the wellheads at the seabed (API RP 2RD, 2006). Exploration and production activities for oil and gas in deep water have increased dramatically in recent years. When the water depth becomes deeper and deeper, the length of a riser also increases. Hence, the design of the deepwater riser system is more challenging than that in shallow water.

There are several options for the adoption of a riser system, such as steel catenary riser (SCR), top tensioned riser (TTR) and flexible riser (FR). Design challenges are faced by these options in terms of vessel payloads and the fatigue performance. For a steel catenary riser (SCR), the fatigue performance at touchdown zone is sensitive to the heave motion of the host vessel. Therefore, a SCR may be not suitable for non-heave optimized vessels, such as FPSO and Semi-Submersible. The top tensioned riser (TTR) is tensioned by a hydraulic tensioner system, which induces the large structural stiffness and hence reduces the riser motion amplitude. However, the top tension given by a tensioner system is typically at least 1.5 times of the wet weight of the TTR. The large vessel payload induced by TTRs is not appropriate for shallow draft vessels. The flexible risers (FR) are composed by several concentric layers of helical metallic armors and polymeric material as shown schematically in Figure 1.1. The metallic armors give mechanical strength to the pipe and the polymer layers are responsible for the pipe‟s

sealing and insulation (Bai and Bai 2005). Due to the multiple layers, the bending stiffness of FR is small, which leads a good fatigue performance. Since the FR cannot stand high external pressure, the water depth is a limitation to avoid the collapse.

Free Standing Hybrid Risers (FSHRs) have been used for many deepwater oil and gas fields in Brazil, West of Africa and Gulf of Mexico. A FSHR mainly consists of a buoyancy can, vertical riser, flexible jumper and upper riser assembly (URA). A buoyancy can tensioning the vertical riser provides required uplift force. For a single line FSHR, the flexible jumper connects the vertical riser to the floating production unit through the URA, which is a loading interface between the buoyancy can, vertical riser and flexible jumper. The connection of the vertical riser to the foundation at the seabed is done by a roto-latch connector. A typical FSHR configuration is illustrated in Figure 1.1 (Song *et al* 2010).

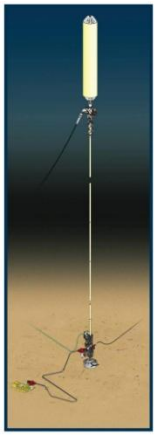

Figure 1.1 Free Standing Hybrid Riser

A FSHR offers several advantages over other types of risers. Firstly, since a buoyancy can supports the weight of the vertical riser, the vessel payload from FSHRs is relatively low. Secondly, the vertical riser is decoupled from the vessel motions due to the use of the small bending stiffness of the flexible jumper. Therefore, the vessel motion induced fatigue damage on the vertical riser is reduced. Thirdly, both buoyancy can and vertical riser locate at about 200m below the water surface where the wave effect is negligible. Finally, a FSHR can be installed ahead of the arrival of the host vessel, thus making the installation schedule more flexible.

COUPLE is a numerical code developed for the coupled dynamic analysis of the rigid floating body moored by mooring lines and attached to risers, for example, a Spar with its mooring and riser system. In this study, several improvements are made to COUPLE to allow for the static and dynamic global analysis of a FSHR. OrcaFlex is a commercial software for the global dynamic analysis of the marine systems. These two codes were used in this study for the numerical simulation of FSHRs.

1.2 Previous Studies

Pereira (2006) carried out numerical simulations for the vertical riser tensioned by a buoyancy can. The hydrodynamic force in the transverse direction currents was calculated using the extended Morison Equation. Hydrodynamic coefficients and oscillation frequency are critical for the riser displacement amplitude. Celso (2012)

continued the works of Pereira (2006) by including the flexible jumper in his numerical models. The results showed that the wave effect on motions of the buoyancy can and vertical riser is insignificant. Related model tests were carried out by Pereira (2005) to investigate the global performance of the FSHR under effects of wave and current. In the experiment, the top of flexible jumper was connected with an enforced oscillator to simulate the motion of vessel. The in-line motion of buoyancy can and vertical riser are smaller than the oscillator due to the use of flexible jumper.

A flow past a buoyancy can may result in vortex shedding, which in turn produces oscillating lift force on the buoyancy can. The vortex induced motion (VIM) of the buoyancy can has impacts on the fatigue damage of the riser. Minguez (2011) studied the VIM and VIR (vortex induced rotation) of a buoyancy can using CFD. At low reduced velocity, the vortex shedding frequency may be close to the natural frequency of the riser system. When increasing the velocity, multi-frequency response is observed from the motion spectrum. The maximum VIM A/D ratio was found to be about 0.9. These findings are consistent with the experimental data of Wilde (2007). Celso (2012) developed a procedure for evaluating the lift coefficient C_L. Different values of C_L are tested in the numerical simulation until the difference between simulated A/D and experimental one is less than 5%. The study provided the non-dimensional curves for the Strouhal number and lift coefficient versus the reduced velocity. These results will be used to evaluate the oscillating force on the buoyancy can in our study.

2. NUMERICAL SCHEME

Mooring lines and risers are long in length and relatively small in diameter or equivalent diameter. Hence, they are modeled by slender rods and the hydrodynamic loads on them are approximately calculated using the Morison equation.

2.1 Simulation of Slender Rods

Equations of motion of a slender rod summarized below, mainly follows the work by Love (1944), Nordgren (1974), Garrett (1982), Paulling and Webster (1986), Ma and Webster (1994) and Chen (2002).

The internal state of stress at a point on the slender rod is described fully by the resultant force **F** and the resultant moment $\widetilde{\mathbf{M}}$ acting at the centerline of the slender rod. On the basis of conservation of linear momentum and moment of momentum, we have equations (2.1) and (2.2):

$$\mathbf{F}' + \mathbf{q} = \rho \ddot{\mathbf{r}}(s,t) \tag{2.1}$$

$$\tilde{\mathbf{M}}' + \mathbf{r}' \times \mathbf{F} + \mathbf{m} = 0 \tag{2.2}$$

where q is the distributed external force along the slender rod per unit length,

ρ is the mass per unit length, and

m is the external moment per unit length.

A superposed dot denotes differentiation with respect to time, while the prime denotes the derivatives with respect to *s*. The effects of rotary inertia and shear deformations are neglected.

For an elastic rod with equal principal stiffness, the bending moment is linearly proportional to curvature and in the direction along the binormal according to the Bernoulli-Euler theory. The resultant moment $\tilde{\mathbf{M}}$ can be written as:

$$\tilde{\mathbf{M}} = \mathbf{r}' \times (B\mathbf{r}'') \tag{2.3}$$

$$\tilde{\mathbf{M}}' = \mathbf{r}' \times (B\mathbf{r}'')' \tag{2.4}$$

Assuming **m**=0, plug $\tilde{\mathbf{M}}'$ (2.4) into equations (2.1) and (2.2), we obtain the following expression for **F**:

$$\mathbf{F} = \lambda\mathbf{r}' - (B\mathbf{r}'')' \tag{2.5}$$

The equation of motion is finally derived by plugging **F** of (2.5) into (2.1):

$$-(B\mathbf{r}'')'' + (\lambda\mathbf{r}')' + \mathbf{q} = \rho\ddot{\mathbf{r}} \tag{2.6}$$

$$T = \mathbf{r}' \cdot \mathbf{F} = \mathbf{r}' \cdot \lambda\mathbf{r}' - \mathbf{r}' \cdot (B\mathbf{r}'')' \tag{2.7}$$

In the derivation the assumption of the small elongation condition was made:

$$\mathbf{r}' \cdot \mathbf{r}' = (1+\varepsilon)^2 \tag{2.8}$$

$$\lambda = \frac{T - B\kappa^2}{(1+\varepsilon)^2} \tag{2.9}$$

where $\kappa^2 = -\mathbf{r}'\cdot\mathbf{r}'''$, κ is the local curvature of the slender rod, and $T(s,t) = \mathbf{r}'\cdot\mathbf{F}$ is the local tension.

The external forces applied on a slender rod consist of gravity forces, hydrostatic and hydrodynamic forces. The gravity force on the rod leads to a distributed load given by:

$$\mathbf{q}_t(s,t) = -\rho_t g A_t \mathbf{e}_y \tag{2.10}$$

The hydrodynamic forces acting on the slender rod consist of added-mass force, drag force, and Froude-Krylov force. The Morison equation is used to predict the first two terms:

$$\mathbf{q}_f^I(s,t) = \rho_f A_f C_{Mn}\mathbf{N}(\mathbf{a}_f - \ddot{\mathbf{r}}) + \rho_f A_f C_{Mt}\mathbf{T}(\mathbf{a}_f - \ddot{\mathbf{r}}) \tag{2.11}$$

$$\begin{aligned}\mathbf{q}_f^D(s,t) = &\frac{1}{2}\rho_f D_f C_{Dn}\mathbf{N}(\mathbf{v}_f - \dot{\mathbf{r}})\left|\mathbf{N}(\mathbf{v}_f - \dot{\mathbf{r}})\right| \\ &+\frac{1}{2}\rho_f D_f C_{Dt}\mathbf{T}(\mathbf{v}_f - \dot{\mathbf{r}})\left|\mathbf{T}(\mathbf{v}_f - \dot{\mathbf{r}})\right|\end{aligned} \tag{2.12}$$

where C_{Mn}, C_{Mt}, C_{Dn} and C_{Dt} are the normal added-mass coefficient, tangential added-mass coefficient, normal drag coefficient and tangential drag coefficient respectively.

Froude - Krylov force due to sea water outside the slender rod is:

$$\mathbf{q}_f^{F-K}(s,t) = \rho_f (g\mathbf{e}_y + \mathbf{a}_f) A_f + (P_f A_f \mathbf{r}')' \tag{2.13}$$

Froude-Krylov force (pressure forces) due to the fluid inside the rod is:

$$\mathbf{q}_i^{F-K}(s,t) = -\rho_i g A_i \mathbf{e}_y - (P_i A_i \mathbf{r}')' \tag{2.14}$$

In the above equations:

$\rho = \rho_t A_t + \rho_i A_i$, the mass per unit length (including the internal fluid),

$\rho_f(s)$ = the mass density of the sea water,

$\rho_i(s)$ = the mass density of the inside fluid,

ρ_t(s) = the mass density of the slender rod,

$A_f(s)$ = the outer cross-section area of the slender rod,

$D_f(s)$ = the diameter of the slender rod,

$A_i(s)$ = the inner cross-section area of the slender rod,

$A_t(s)$ = the structural cross-section area of the slender rod,

$\mathbf{v}_f$ = the velocity of the sea water (current and wave),

$\mathbf{a}_f$ = the acceleration of the sea water (current and wave),

P_f = pressure of the sea water,

P_i = pressure of the internal fluid,

T, **N** = transfer matrices,

I = identity matrix,

where the subscripts *f*, *i* and *t* denote the sea water, the fluid inside the tube and the tube itself. **T** and **N** are defined by:

$$\mathbf{T} = \mathbf{r}'^{T}\mathbf{r}' \tag{2.15}$$

$$\mathbf{N} = \mathbf{I} - \mathbf{T} \tag{2.16}$$

The governing equation is finally obtained as:

$$\mathbf{M}\ddot{\mathbf{r}} + (B\mathbf{r}'')'' - (\tilde{\lambda}\mathbf{r}')' = \mathbf{q} \tag{2.17}$$

where

$$\begin{aligned}\mathbf{q} = {} & (\rho_f A_f - \rho_i A_i - \rho_t A_t)g\mathbf{e}_y + \rho_f A_f(\mathbf{I} + C_{Mn}\mathbf{N} + C_{Mt}\mathbf{T})\mathbf{a}_f \\ & + \frac{1}{2}\rho_f D_f C_{Dn}\mathbf{N}(\mathbf{v}_f - \dot{\mathbf{r}})\left|\mathbf{N}(\mathbf{v}_f - \dot{\mathbf{r}})\right| \\ & + \frac{1}{2}\rho_f D_f C_{Dt}\mathbf{T}(\mathbf{v}_f - \dot{\mathbf{r}})\left|\mathbf{T}(\mathbf{v}_f - \dot{\mathbf{r}})\right|\end{aligned} \tag{2.18}$$

the virtual mass matrix:

$$\mathbf{M} = (\rho_t A_t + \rho_i A_i)\mathbf{I} + \rho_f A_f C_{Mn}\mathbf{N} + \rho_f A_f C_{Mt}\mathbf{T} \tag{2.19}$$

$$\tilde{\lambda} = \lambda + P_f A_f - P_i A_i = \frac{T - B\kappa^2}{(1+\varepsilon)^2} + P_f A_f - P_i A_i \tag{2.20}$$

and assume curvature κ is small, then ε can expressed as:

$$\varepsilon = \frac{T}{EA} \approx \frac{\tilde{\lambda} - P_f A_f + P_i A_i}{EA} \tag{2.21}$$

The term in the parentheses in equation (2.20) is known as the “effective tension”.

The Galerkin's method is adopted to discretize the partial differential equations of motion from (2.17), and the constraints equations (2.8) and (2.21) in space, resulting in a set of nonlinear 2nd-order ordinary differential equations in the time domain.

Equation (2.17) may be reduced to a set of ordinary differential equations using Galerkin's method. Multiplying both side of the equation by $a_i(s)$ and integrating it with respect to s from 0 to L for an element of the length of L:

$$\int_0^L \left\{ \mathbf{M}\ddot{\mathbf{r}} + (B\mathbf{r}'')'' - (\tilde{\lambda}\mathbf{r}')' - \mathbf{q} \right\} a_i(s)\, ds = 0 \tag{2.22}$$

where the Hermite cubic shape function $a(s)$ are:

$$\begin{aligned} a_1(\xi) &= 1 - 3\xi^2 + 2\xi^3 \\ a_2(\xi) &= \xi - 2\xi^2 + \xi^3 \\ a_3(\xi) &= 3\xi^2 - 2\xi^3 \\ a_4(\xi) &= -\xi^2 + \xi^3 \end{aligned} \tag{2.23}$$

Integrating the above equation by parts results in equation (2.24):

$$\begin{aligned} &\int_0^L \left\{ \mathbf{M}\ddot{\mathbf{r}} a_i(s) + B\mathbf{r}'' a_i''(s) + \tilde{\lambda}\mathbf{r}' a_i'(s) - \mathbf{q}\, a_i(s) \right\} ds \\ &= B\mathbf{r}''\, a_i'(s)\Big|_o^L + \left\{ \tilde{\lambda}\mathbf{r}' - (B\mathbf{r}'')' \right\} a_i(s)\Big|_0^L \end{aligned} \tag{2.24}$$

The first term on the right-hand side of the equation is related to the moments at the ends of the element, and the second term (in curly brackets) is the forces at the ends of the element. The right-hand side terms are called generalized forces $\mathbf{f}_i$, which can be expressed as:

$$\mathbf{f}_i = B\mathbf{r}''\, a'_i\Big|_o^L + \left\{ \tilde{\lambda}\mathbf{r}' - (B\mathbf{r}'')' \right\} a_i\Big|_0^L,\ i = 1,2,3,4 \tag{2.25}$$

$$\mathbf{f}_1 = -\left\{ \tilde{\lambda}\mathbf{r}'(0) - (B\mathbf{r}'')'(0) \right\} = -\mathbf{F}(0) \tag{2.26}$$

$$\mathbf{f}_2 = -\frac{1}{L} B\mathbf{r}''(0) = \frac{1}{L}\mathbf{r}'(0) \times \tilde{\mathbf{M}}(0) \tag{2.27}$$

$$\mathbf{f}_3 = \left\{ \tilde{\lambda}\mathbf{r}'(L) - (B\mathbf{r}'')'(L) \right\} = \mathbf{F}(L) \tag{2.28}$$

$$\mathbf{f}_4 = \frac{1}{L} B\mathbf{r}''(0) = -\frac{1}{L}\mathbf{r}'(L) \times \tilde{\mathbf{M}}(L) \tag{2.29}$$

The details of adopting shape functions to discretize the motion equation and constraints equation could be found in Chen (2002). After assemble the equations of each element into a global form $A\delta X = B$, different boundary conditions should be added into the global equations, which are discussed in following sections.

2.2 Boundary Conditions of Slender Structures

At the first and last node of each slender rod, it is necessary to assign boundary conditions based on the description of related physical constraints, such as hinge connection, rotational spring connection, etc, which will be discussed and formulated in the following subsections. Rewriting equation (2.24) in the form of equation (2.30), where $\mathbf{f}_i$ was defined in equations (2.25) – (2.29). According to the description of physical constraints at the boundary nodes, appropriate boundary conditions are derived for the variables, such as $\mathbf{r}, \mathbf{r}'$, and $\mathbf{f}_i$, or their relations.

$$\int_0^L \left\{ \mathbf{M}\ddot{\mathbf{r}} a_i(s) + B\mathbf{r}'' a_i''(s) + \tilde{\lambda}\mathbf{r}' a_i'(s) - \mathbf{q}\, a_i(s) \right\} ds = \mathbf{f}_i \tag{2.30}$$

2.2.1 Hinged Boundary Condition

A fairlead is the link between the upper end of a mooring line and the related floater, and it is usually modeled as a hinge connection. The boundary condition for a hinge connector was available in the original version of COUPLE and hence is briefly

described here. A hinge connector virtually allows free rotation and the related bending moment at the connection point is zero. However, the displacement and the tension at the first node of the related slender rod match with those at the same location of the related floater. In the numerical scheme of COUPLE, the hinged boundary condition means $\mathbf{f}_2$ (bending moment) is equal to zero and $\mathbf{r}$ matches the coordinates of the related floater at the hinge connector.

2.2.2 Rotational Spring Boundary Condition

In general, a Steel Catenary Riser (SCR) is connected with the related floater through a Flex Joint to allow certain rotations between the SCR and floater at the porch. In this case, the boundary condition of a SCR at the porch is modeled by a rotational spring. The bending moment acting at the upper end of a slender rod is determined by the multiplication of the rotational stiffness (of a Flex Joint) and the relative angle, which is the angle between the neutral vector of the Flex Joint and the tangential vector at the upper end of the SCR. By definition, the bending moment is equal to zero when the neutral vector of the Flex Joint and the tangential vector of the SCR at its upper end is coincident. In general, when a floater is in its equilibrium position, the two vectors are coincident.

Mathematically, the rotational spring boundary condition at the porch are given below.

$$\tilde{\mathbf{M}} = M_0 \boldsymbol{\theta} \quad \text{at} \quad \mathbf{s}=0 \tag{2.31}$$

where M_0 represents the linear rotational stiffness of the rotational spring, which is an input, depending the property of a Flex Joint used at the porch; $\boldsymbol{\theta}$ is the relative angle between the neutral vector and the tangential vector and it is a function of $\mathbf{r}'$ and the orientation of the floater.

$$\begin{aligned}\mathbf{f}_2 &= -\frac{1}{L}B\mathbf{r}'' = \frac{1}{L}\mathbf{r}'\times\tilde{\mathbf{M}} = \frac{M_0}{L}\mathbf{r}'\times\boldsymbol{\theta} \\ &= \frac{M_0}{L}(\mathbf{r}'^0+\delta\mathbf{r}')\times(\boldsymbol{\theta}^0+\delta\boldsymbol{\theta}) = \mathbf{[a]}\delta\mathbf{r}'+\mathbf{[b]}\end{aligned} \tag{2.32}$$

Substituting equation (2.31) into equation (2.27), we obtain (2.32), which is used to compute $\mathbf{f}_2$. [**a**] is the 3×3 coefficient matrix related to $\delta\mathbf{r}'$ and [**b**] is the 3×1 coefficient matrix related to $\mathbf{r}'^0$. $\mathbf{r}'^0$ is the initial guess (predictor) and $\delta\mathbf{r}'$ is the corrector. Recalling that the global equations $[A][\delta X]=[B]$, $[A]$ is the coefficient matrix and $[\delta X]$ the unknown increment or corrector. By adding [**a**] and [**b**] into $[A]$ and $[B]$, respectively, the rotational spring boundary condition is considered in the computation. Detailed derivation of the coefficient matrices [**a**] and [**b**] is presented in Appendix I. It should be noted that an earlier derivation of the rotational spring boundary condition was given by Huang (2013). He used the Taylor expansion to approximate the relative angle and the computation may not converge when the rotational stiffness is smaller than but close to the bending stiffness of the SCR. The rotational spring boundary condition derived in Appendix I eliminates the convergence difficulty.

2.2.3 Clamped Boundary Condition

In the case of the connection between the vertical riser and upper riser assembly, a stress joint is applied. The stress joint is typically modeled as the clamped boundary condition. In other words, the rotational stiffness of a clamped boundary is practically equal to the bending stiffness of the vertical riser. It should be noted the rotation stiffness of a Flex Joint is usually significantly smaller than the related bending stiffness of the riser. Hence, the clamped boundary condition can be viewed as a special case as a rotational spring, in which M_0 is equal to the bending stiffness of the riser.

2.2.4 Free Boundary Condition

When there is no tension and bending moment applied at the end of a slender rod, the boundary condition is known as the free boundary condition. That is, the end of a slender rod is free to move and rotate. Therefore, $\mathbf{r}''$, , $\mathbf{f}_1$ and $\mathbf{f}_2$ at s=0 are zero in equation (2.30).

2.3 Coupled Analysis of the Free Standing Hybrid Riser

A FSHR consists of four main components. They are the buoyancy can (with tether chain connecting the buoyancy can to the URA), vertical riser, flexible jumper and

upper riser assembly (URA). The buoyancy can (with tether chain), vertical riser and flexible jumper are modeled as slender rods. The URA is modeled as a rigid body. Numerical simulation of each component is described in the following subsections.

2.3.1 Buoyancy Can and Tether Chain

The buoyancy can is connected to the upper riser assembly via a tether chain. The buoyancy can and tether chain are together modeled as a slender rod. In the same slender rod, the buoyancy can is modeled by a beam element and the upper end of the buoyancy can is considered as a free end. The tether chain is modeled by several bar elements (without bending stiffness). The connection between the tether chain and URA is modeled by the hinged boundary condition.

2.3.2 Vertical Riser

The vertical riser is modeled using beam elements. The tension and bending stiffness of the beam element is equivalent to those of the same cross-section of the steel pipe. The insulation layer is also considered when calculating the mass, buoyancy and hydrodynamic loads.

Typically, a stress joint is selected to be the connector between the upper riser assembly and the vertical riser. The stress joint is modeled by the clamped boundary at the upper end of the vertical riser.

At the lower end of the vertical riser, a Roto-Latch connector is used to attach the vertical riser to the suction pile. The boundary condition of the vertical riser at the Roto-Latch is modeled by a rotational spring with the prescribed rotational stiffness.

2.3.3 Flexible Jumper

The flexible jumper is modeled by beam elements with prescribed small bending stiffness and relatively large tension stiffness. The stiffness is given according to the properties of the flexible jumper.

A gooseneck assembly is to connect the flexible jumper with the upper riser assembly. The boundary conditions at both ends of the flexible jumper are modeled as clamped boundary conditions. The rotational stiffness is the bending stiffness of the flexible jumper.

2.3.4 Upper Riser Assembly

The upper riser assembly is a truss type structure which hosts a steel pipe. It serves as an interface between the flexible jumper and vertical riser. Because of its large tension and bending stiffness, the URA is modeled as a rigid body.

2.3.4.1 Hydrodynamic Loads

A URA usually locates at least 150m below the water surface, where the wave kinematics and wave induced pressure are insignificant. An URA is relatively long and small in horizontal dimension. Hence, the Morison equation is a good approximation to compute hydrodynamic loads on the URA due to the currents and its own motions. The motion equations incorporating with the use of Morison equation mainly follow Chen (2002). Detailed derivation of the hydrodynamic loads is described in CHAPTER 3.4 of Chen (2002).

2.3.4.2 Loads from Slender Rods

Numerical simulation of the loads contributed from slender rods on an URA follows Chen (2002). However, Chen only considered the hinged boundary condition for slender rods. On the other hand, the FSHR contains the rotational spring and clamped boundary conditions in addition to hinge boundary conditions. When there is a bending moment applied on a riser end, the force is contributed by both the tension and shear force. Therefore, the computation of the loads applied at the beam element end is modified in COUPLE.

Since the coordinates are different for the slender rods and the rigid body, each coordinate system needs to be described. $O'X'Y'Z'$ is the global coordinate system for slender rods (such as the buoyancy can, vertical riser and flexible jumper), with origin O'

at the water surface and Y' axis positive upward. $OXYZ$ is the global coordinate system for the rigid body (URA), with origin O at the water surface and Z axis positive upward. O' and O are coincident. The horizontal coordinates of the lower end of the vertical riser in both global coordinate systems are (0, 0). $oxyz$ is the body-fixed coordinate system of the rigid body (see Figure 2.1). The origin o is located at the center of gravity of the URA.

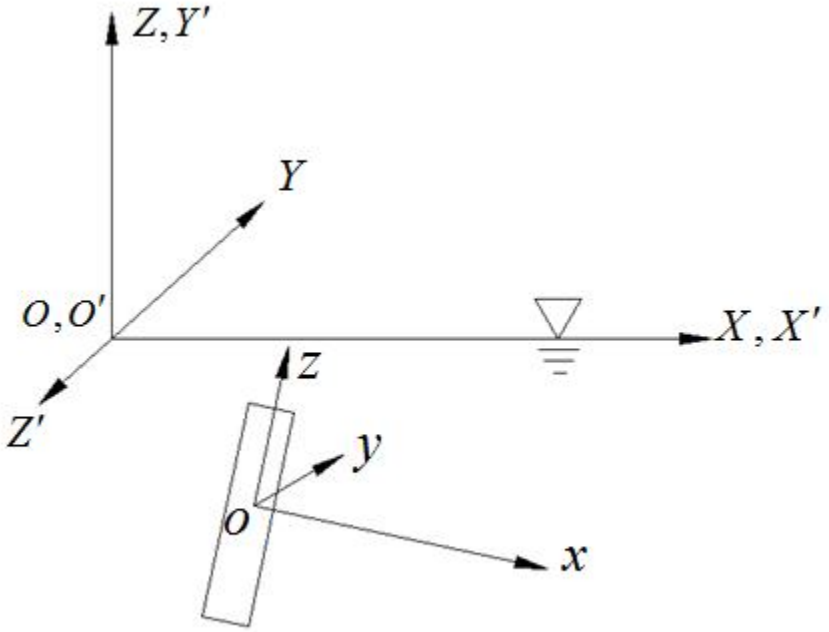

Figure 2.1 Coordinate systems

$\mathbf{x}_{cl}$ are the coordinates of the connector point (porch and fairlead) at the URA expressed in body-fixed coordinate system. $\mathbf{r}_{0l}$ are the coordinates of the connector point

of *lth* slender rod expressed in global coordinate system *O'X'Y'Z'*. They have the relationship in equation (2.33).

$$\mathbf{r}_{0l} = \mathbf{L}^l(\mathbf{T}^l\mathbf{x}_{cl} + \mathbf{X}_o + \boldsymbol{\xi}) \tag{2.33}$$

In the above equation,

T is the matrix considering the rotation of the rigid body.

$$\mathbf{T} = \begin{bmatrix} \cos\alpha_3\cos\alpha_2 & \sin\alpha_3\cos\alpha_1 + \cos\alpha_3\sin\alpha_2\sin\alpha_1 & \sin\alpha_3\sin\alpha_1 - \cos\alpha_3\sin\alpha_2\cos\alpha_1 \\ -\sin\alpha_3\cos\alpha_2 & \cos\alpha_3\cos\alpha_1 - \sin\alpha_3\sin\alpha_2\sin\alpha_1 & \cos\alpha_3\sin\alpha_1 + \sin\alpha_3\sin\alpha_2\cos\alpha_1 \\ \sin\alpha_2 & -\cos\alpha_2\sin\alpha_1 & \cos\alpha_2\cos\alpha_1 \end{bmatrix} \tag{2.34}$$

α_1, α_2 and α_3 are the rotation angles with respect to *x*, *y* and *z*-axis, respectively, in the body-fixed coordinate system of the rigid body.

$\mathbf{X}_o$ are the initial coordinates of the origin of the body-fixed coordinate system expressed in the global coordinate system *OXYZ*.

$\boldsymbol{\xi}$ is the translational motion of the origin of the body-fixed coordinate system also expressed in *OXYZ*.

L is the transfer matrix between *OXYZ* and *O'X'Y'Z'*.

$$L = \begin{Bmatrix} 1 & 0 & 0 \\ 0 & 0 & -1 \\ 0 & 1 & 0 \end{Bmatrix} \tag{2.35}$$

$$\begin{Bmatrix} X \\ Y \\ Z \end{Bmatrix} = L \begin{Bmatrix} X' \\ Y' \\ Z' \end{Bmatrix} \tag{2.36}$$

The generalized forces and moments applied at the connection point (s=0) of lth slender rod are computed by equations (2.37) and (2.38).

$$\mathbf{f}_1 = -\left\{\tilde{\lambda}\mathbf{r}'(0) - (B\mathbf{r}'')'(0)\right\} = -\mathbf{F}(0) \tag{2.37}$$

$$\mathbf{f}_2 = -\frac{1}{L}B\mathbf{r}''(0) = \frac{1}{L}\mathbf{r}'(0) \times \tilde{\mathbf{M}}(0) \tag{2.38}$$

Forces expressed in the global coordinate system of slender structures, $O'X'Y'Z'$, applied on the URA at lth connection point (s=0) are evaluated by equation (2.39). $\tilde{\lambda}$ and $\mathbf{r}'$ are solved at each time step, while $\mathbf{r}'''$ is evaluated using the forward difference scheme. B is the bending stiffness of the beam element. Bending moment is computed by the rotational spring model.

$$\mathbf{F}_l = \mathbf{F}(0) = \tilde{\lambda}\mathbf{r}'(0) - (B\mathbf{r}'')'(0) \tag{2.39}$$

$$\tilde{\mathbf{M}}_l = \tilde{\mathbf{M}}(0) \tag{2.40}$$

Loads from slender rods applied on the URA are the summation of forces and moments of each slender rod at the respective connection points. Since the translational motion of the rigid body is solved in the global coordinate system, $\hat{F}_{slender}$ is expressed in the global coordinate system $OXYZ$. Since the rotation of the rigid body is solved in the body-fixed coordinate system, $\mathbf{M}_{slender}$ is expressed in the body-fixed coordinate system $oxyz$.

$$\hat{\mathbf{F}}_{slender} = \sum_{l=1}^{L}(\mathbf{L}\mathbf{F}_l) \tag{2.41}$$

$$\mathbf{M}_{slender} = \sum_{l=1}^{L} \left[\mathbf{r}_{cl} \times (\mathbf{TLF}_l) + \mathbf{TL}\tilde{\mathbf{M}}_l \right] \tag{2.42}$$

2.3.4.3 Summary of Motion Equation

The 6-DOF motion equation (2.43) of the rigid body is based on Newton Second Law. Knowing the loads from slender rods and hydrodynamic loads, the acceleration of the URA can be solved at each time step. Knowing the motion of the URA, the boundary conditions at the connection between slender rods and the URA are determined. By this approach, the dynamics of the risers and URA are coupled and solved together.

$$[\mathbf{M}]\ddot{\mathbf{x}}(t) = \mathbf{F}_{hydrodynamic} + \mathbf{F}_{slender} + \mathbf{F}_{steady} \tag{2.43}$$

2.3.5 Numerical Simulation

2.3.5.1 Static Analysis

The static equilibrium position of the FSHR is solved using Newton‟s method. In the static equilibrium position, the URA experiences no dynamic forces.

$$0 = \mathbf{F}_{steady} + \mathbf{F}_{slender}, \tag{2.44}$$

where $\mathbf{F}_{steady}$ is the steady force including the gravity, buoyancy and current loads applied on the URA and $\mathbf{F}_{slender}$ the forces applied by thether chain, vertical riser and

flexible jumper. Based on Newton‟s method (2.45), equation (2.46) can be derived from equation (2.44).

$$\mathbf{x} = \mathbf{x}^0 + \delta\mathbf{x} \tag{2.45}$$

$$\frac{\partial \mathbf{F}_{slender}}{\partial \mathbf{x}} \delta\mathbf{x} = \mathbf{F}_{steady} + \mathbf{F}_{slender}{}^0 \tag{2.46}$$

The equation is solved in the following steps.

Step 1: At the initial position of the URA, the boundary conditions at the connections of slender rods are given. Then $\frac{\partial \mathbf{F}_{slender}}{\partial \mathbf{x}}$ and $\mathbf{F}_{slender}{}^0$ are calculated at the initial position.

Step 2: After solving equation (2.46) for $\delta\mathbf{x}$, $\mathbf{x}$ is updated following equation (2.45). $\frac{\partial \mathbf{F}_{slender}}{\partial \mathbf{x}}$ is a 6 by 6 stiffness matrix, which is updated at each position of the URA, $\mathbf{x}$.

Step 3: If $\delta\mathbf{x}$ satisfies the convergence criteria, the static analysis is finished, otherwise go to Step 2 iteratively.

2.3.5.2 Dynamic Analysis

The governing equation for the motion of the URA is given below.

$$[\mathbf{M}]\ddot{\mathbf{x}}(t) = \mathbf{F}_{hydrodynamic} + \mathbf{F}_{slender} + \mathbf{F}_{steady}, \tag{2.47}$$

and the dynamic equation of a slender rod is given below.

$$\int_0^L \left\{ \mathbf{M}\ddot{\mathbf{r}} a_i(s) + B\mathbf{r}'' a_i''(s) + \tilde{\lambda}\mathbf{r}' a_i'(s) - \mathbf{q}\, a_i(s) \right\} ds = \mathbf{f}_i \tag{2.48}$$

$\mathbf{F}_{slender}$ in equation (2.47) and $\mathbf{f}_i$ in equation (2.48) are related through equations (2.37) - (2.42). In the coupled dynamic analysis, Newmark-β method is used to solve the above equations for the URA and slender rods simultaneously. The numerical scheme for solving equation (2.47) mainly follows Chen (2002), except that in this study the increment of the acceleration of the URA is solved instead of the increment of the displacement.

Step 1: At t=0 (or time step K=0), a dynamic analysis starts from the static equilibrium position of the system. For the rigid body, $\ddot{\mathbf{x}}^{(K)} = 0$ and $\dot{\mathbf{x}}^{(K)} = 0$. For slender rods, $\ddot{\mathbf{r}}^{(K)} = 0$ and $\dot{\mathbf{r}}^{(K)} = 0$.

Step 2: At time step K (>0), $\mathbf{x}^{(K)}$, $\dot{\mathbf{x}}^{(K)}$ and $\ddot{\mathbf{x}}^{(K)}$ of the rigid body are predicted by Newmark-β method in equation (2.49).

$$\begin{aligned}
\ddot{\mathbf{x}}^{(K)} &= \ddot{\mathbf{x}}^{(K-1)} \\
\dot{\mathbf{x}}^{(K)} &= \dot{\mathbf{x}}^{(K-1)} + \Delta t(1-\gamma)\ddot{\mathbf{x}}^{(K-1)} + \Delta t\gamma\ddot{\mathbf{x}}^{(K)} \\
\mathbf{x}^{(K)} &= \mathbf{x}^{(K-1)} + \Delta t\dot{\mathbf{x}}^{(K-1)} + \Delta t^2(\frac{1}{2}-\beta)\ddot{\mathbf{x}}^{(K-1)} + \Delta t^2\beta\ddot{\mathbf{x}}^{(K)}
\end{aligned} \tag{2.49}$$

Similarly, $\mathbf{r}^{(K)}$, $\dot{\mathbf{r}}^{(K)}$, $\ddot{\mathbf{r}}^{(K)}$ and $\tilde{\lambda}^{(K)}$ of slender rods are given below.

$$
\begin{aligned}
\ddot{\mathbf{r}}^{(K)} &= \ddot{\mathbf{r}}^{(K-1)} \\
\dot{\mathbf{r}}^{(K)} &= \dot{\mathbf{r}}^{(K-1)} + \Delta t(1-\gamma)\ddot{\mathbf{r}}^{(K-1)} + \Delta t\gamma\ddot{\mathbf{r}}^{(K)} \\
\mathbf{r}^{(K)} &= \mathbf{r}^{(K-1)} + \Delta t\dot{\mathbf{r}}^{(K-1)} + \Delta t^2(\frac{1}{2}-\beta)\ddot{\mathbf{r}}^{(K-1)} + \Delta t^2\beta\ddot{\mathbf{r}}^{(K)} \\
\tilde{\lambda}^{(K)} &= \tilde{\lambda}^{(K-1)}
\end{aligned}
\tag{2.50}
$$

Step 3: Based on Newton"s method and Newmark-β method, equation (2.47) can be rewritten as equation (2.51). The increment of acceleration of the rigid body, $\delta\ddot{\mathbf{x}}^{(K)}$, is solved at time step *K*.

$$
\left[\mathbf{M} - \frac{\partial \mathbf{F}_{slender}}{\partial \mathbf{x}}\Delta t^2\beta\right]\delta\ddot{\mathbf{x}}^{(K)} = \mathbf{F}^{(K)}_{hydrodynamic} + \mathbf{F}^{(K)}_{slender} + \mathbf{F}_{steady} - \left[\mathbf{M}\right]\ddot{\mathbf{x}}^{(K)} \tag{2.51}
$$

To solve equation (2.48), boundary conditions of each slender rod at the step *K*, are applied. After obtaining $\mathbf{F}^{(K)}_{slender}$ based on $\mathbf{f}_i$ at each connection point, $\delta\ddot{\mathbf{x}}^{(K)}$ in equation (2.51) can be solved.

Step 4: The corrector of $\mathbf{x}^{(K)}$, $\dot{\mathbf{x}}^{(K)}$ and $\ddot{\mathbf{x}}^{(K)}$ are given by:

$$
\begin{aligned}
\ddot{\mathbf{x}}^{(K)} &= \ddot{\mathbf{x}}^{(K)} + \delta\ddot{\mathbf{x}}^{(K)} \\
\dot{\mathbf{x}}^{(K)} &= \dot{\mathbf{x}}^{(K)} + \gamma\ \Delta t\ \delta\ddot{\mathbf{x}}^{(K)} \\
\mathbf{x}^{(K)} &= \mathbf{x}^{(K)} + \beta\ \Delta t^2\delta\ddot{\mathbf{x}}^{(K)}
\end{aligned}
\tag{2.52}
$$

Since the increment of $\mathbf{r}^{(K)}$ is solved in computing the slender rod dynamics, $\mathbf{r}^{(K)}$, $\dot{\mathbf{r}}^{(K)}$, $\ddot{\mathbf{r}}^{(K)}$ and $\tilde{\lambda}^{(K)}$ are updated by:

$$
\begin{aligned}
\mathbf{r}^{(K)} &= \mathbf{r}^{(K)} + \delta\mathbf{r}^{(K)} \\
\dot{\mathbf{r}}^{(K)} &= \dot{\mathbf{r}}^{(K)} + \frac{\gamma}{\beta\Delta t}\delta\mathbf{r}^{(K)} \\
\ddot{\mathbf{r}}^{(K)} &= \ddot{\mathbf{r}}^{(K)} + \frac{1}{\beta\Delta t^2}\delta\mathbf{r}^{(K)} \\
\tilde{\lambda}^{(K)} &= \tilde{\lambda}^{(K)} + \delta\tilde{\lambda}^{(K)}
\end{aligned}
\tag{2.53}
$$

When the convergence criteria of $\delta\ddot{\mathbf{x}}^{(K)}$, $\delta\mathbf{r}^{(K)}$ and $\delta\tilde{\lambda}^{(K)}$ are satisfied, the dynamic analysis for the next time step are started.

3. CASES STUDIED

There are two Free Standing Hybrid Risers simulated in this study. In Case I, the FSHR is based on that used in the Roncador P-52 oil export system (Roveri *et al.*2008). It connects the P-52 floating production unit (FPSO) to the pipeline system located in the Campos Basin, offshore Brazil. The water depth is 1800m. It is of the type of a single vertical steel pipe. The riser is tensioned by a buoyancy can, which is mechanically connected to the top of the vertical steel pipe via a tether chain. A gooseneck assembly is located on top of the URA. A flexible jumper links the gooseneck to the FPSO. Figure 3.1 shows the general arrangement of the FSHR. In Case II, the FSHR follows the design by Rombado *et al* (2012). The water depth is 3000m. In summary, the FSHR in Case I is an example deployed in the deep water, while that in the Case II in the ultra-deep water. Rombado *et al* (2012) considered a steel catenary jumper in his study. In this study, a flexible jumper is used instead of the steel catenary jumper. The other properties of the riser system follow Rombado *et al* (2012).

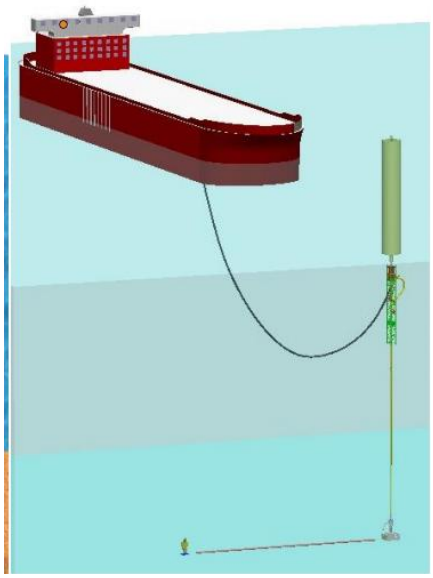

Figure 3.1 FSHR general arrangement

The properties of the buoyancy can and tether chain of the two cases are listed in Tables 3.1 and 3.2, respectively. Those of the vertical risers and flexible jumper are presented, respectively, in Tables 3.3 and 3.4. Those data are used as the input to COUPLE and OrcaFlex.

Table 3.1 Properties of buoyancy can

	Unit	Case I	Case II
Outer Diameter	(m)	5.45	6.4
Length	(m)	34.2	38.4
Net Uplift	(kg)	536000	710000
Drag Coefficient		1.2	1.2
Added Mass Coefficient		1	1

Table 3.2 Properties of tether chain

	Unit	Case I	Case II
Hydrodynamic Diameter	(m)	0.1	0.121
Mass per Unit Length	(kg/m)	60	90
Buoyancy per Unit Length	(kg/m)	8.050333	11.7868
Tension Stiffness	(kN)	250000	413696
Drag Coefficient		1.2	1.2
Added Mass Coefficient		1	1
Length	(m)	10	15

Table 3.3 Properties of vertical riser

	Unit	Case I	Case II
Hydrodynamic Diameter	(m)	0.5572	0.665
Inner Diameter	(m)	0.42545	0.229
Inner Fluid Density	(kg/m^3)	841	841
Mass per Unit Length	(kg/m)	285	437
Buoyancy per Unit Length	(kg/m)	249.9406	355.9625
Bending Stiffness	(kN*m^2)	113000	73289.3
Tension Stiffness	(kN)	4620000	7742000
Drag Coefficient		1.2	1.2
Added Mass Coefficient		1	1
Length	(m)	1580	2490

Table 3.4 Properties of flexible jumper

	Unit	Case I	Case II
Hydrodynamic Diameter	(m)	0.5355	0.5355
Inner Diameter	(m)	0.4064	0.4064
Inner Fluid Density	(kg/m^3)	841	841
Mass per Unit Length	(kg/m)	336.7	336.7
Buoyancy per Unit Length	(kg/m)	224.8597	224.8597
Bending Stiffness	(kN*m^2)	2500	2500
Tension Stiffness	(kN)	1137920	1137920
Drag Coefficient		1.2	1.2
Added Mass Coefficient		1	1
Length	(m)	425	1100

The URA has a truss type structure mainly consisting of five cylinders as shown in Figure 3.2. The detailed information of the truss is not available to us. Assume the URA consisting of the truss and the pipe in the middle rigid, we approximated it as a slender cylinder in the simulation. The equivalent hydrodynamic diameter, added mass coefficient and drag coefficient of the rigid cylinder are such determined that they are equivalent to the corresponding summations of the truss and middle pipe. It is also assumed that the rigid cylinder is homogeneous and the center of gravity is at the geometry center. The input data for URA is summarized below.

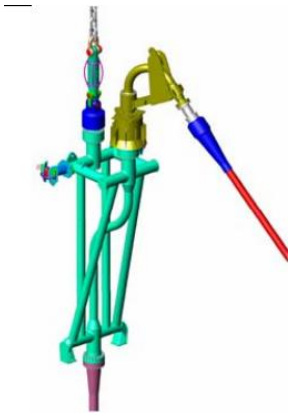

Figure 3.2 Upper Riser Assembly

Table 3.5 Properties of URA

	Unit	Case I	Case II
Mass	(kg)	30000	30000
Hydrodynamic Diameter	(m)	1.02233	1.02233
Drag Coefficient		2.236068	2.236068
Added Mass Coefficient		1	1
Length	(m)	10	10

The origin of the global coordinate system is at the water surface. The origin of the body-fixed coordinate system is at the center of gravity of URA. The positions of the ends of each slender rods are listed in the table below. Static analysis is performed to find out the static equilibrium position of the FSHR system.

Table 3.6 Coordinates of the ends of slender rods for Case I

	Position of the connection on URA (expressed in body-fixed coordinate system)			Position of the other end (expressed in global coordinate system)		
	x (m)	y (m)	z (m)	X (m)	Y (m)	Z (m)
Buoyancy Can and Tether Chain	0.0	0.0	5.0	Free		
Vertical Riser	0.0	0.0	-5.0	0.0	0.0	-1800.0
Flexible Riser	4.0	0.0	0.0	300.0	0.0	0.0

Table 3.7 Coordinates of the ends of slender rods for Case II

	Position of the connection on URA (expressed in body-fixed coordinate system)			Position of the other end (expressed in global coordinate system)		
	x (m)	y (m)	z (m)	X (m)	Y (m)	Z (m)
Buoyancy Can and Tether Chain	0.0	0.0	5.0	Free		
Vertical Riser	0.0	0.0	-5.0	0.0	0.0	-3000.0
Flexible Riser	-2.0	0.0	0.0	-600.0	0.0	0.0

The bottom end of the vertical riser in both cases is modeled by a rotational spring, while the top end of the vertical riser connected to the URA through a stress joint which is modeled by the clamped. The neutral vectors (zero-moment direction) of the clamp and rotational spring are vertical and tangential vectors there are coincident with the corresponding neutral vectors when the URA is at its „initial" position (that is, before the flexible jumper is connected). After the jumper is connected, the tangential vectors at

the top and bottom of the vertical riser will rotate and no longer coincident with the corresponding neutral vectors. The rotational stiffness of the clamp connector is the same as the bending stiffness of the vertical riser, and that of the flex-joint at the bottom end is assumed to be 34.9 kN·m/degree.

The two ends of the flexible jumper connect the URA and the FPSO, respectively. Both connectors are modeled by clamps. The neutral vectors are coincident with the corresponding tangential vectors at both ends when the FSHR is at its static equilibrium position and the rotational stiffness is the same as the bending stiffness of the flexible jumper.

4. NUMERICAL RESULTS

4.1 Equilibrium Position

In absence of wave, current and the motion of the surface vessel (FPSO), the equilibrium positions of two FSHRs are calculated using COUPLE and OrcaFlex, respectively. The results are presented in this section.

4.1.1 Case I

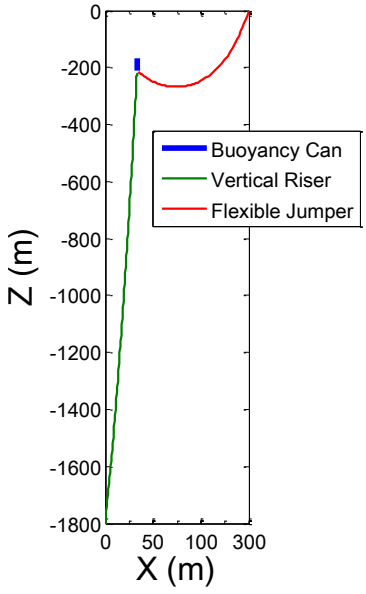

Figure 4.1 Schematic configuration of the static equilibrium position

Table 4.1 Equilibrium position of the center of gravity of URA

	COUPLE		OrcaFlex	
	Without Flexible Jumper	With Flexible Jumper	Without Flexible Jumper	With Flexible Jumper
X (m)	0	65.055	0	65.03
Y (m)	0	0	0	0
Z (m)	-215	-215.313	-215	-215.15
Pitch Angle (degree)	0	1.746	0	1.747

In Case I, one beam element is used to simulate the buoyancy can. The tether chain is discretized into 10 bar elements. The vertical riser is discretized into 106 beam elements. The flexible jumper is discretized into 76 beam elements. Finer meshes are necessary at the region with large curvature and near the boundary. This discretization can lead a convergent result.

Figure 4.1 shows static equilibrium position of the FSHR. Table 4.1 provides the coordinates of the center of gravity of the URA. It is noted that the static force applied by the flexible jumper is in the positive X-direction and hence the offset of the URA is also in the same direction. The difference between the offsets of the URA calculated respectively using COUPLE and OrcaFlex is tiny, only 0.025m.

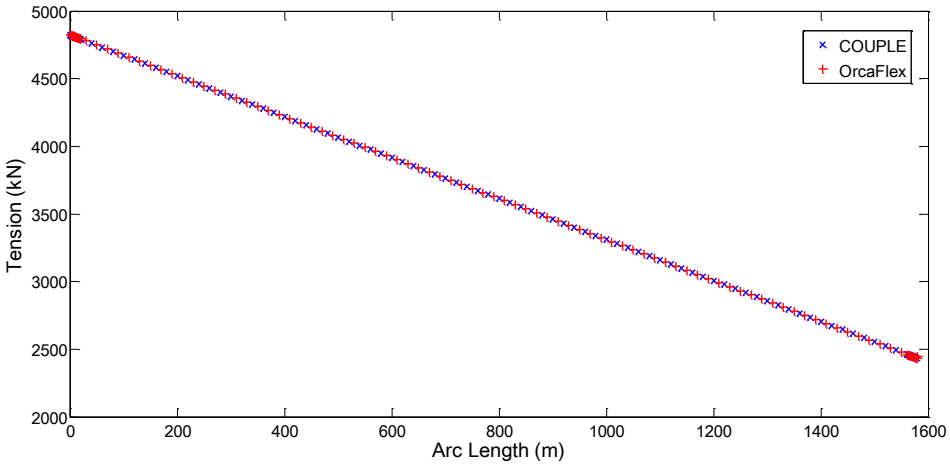

Figure 4.2 Tension along the vertical riser of Case I

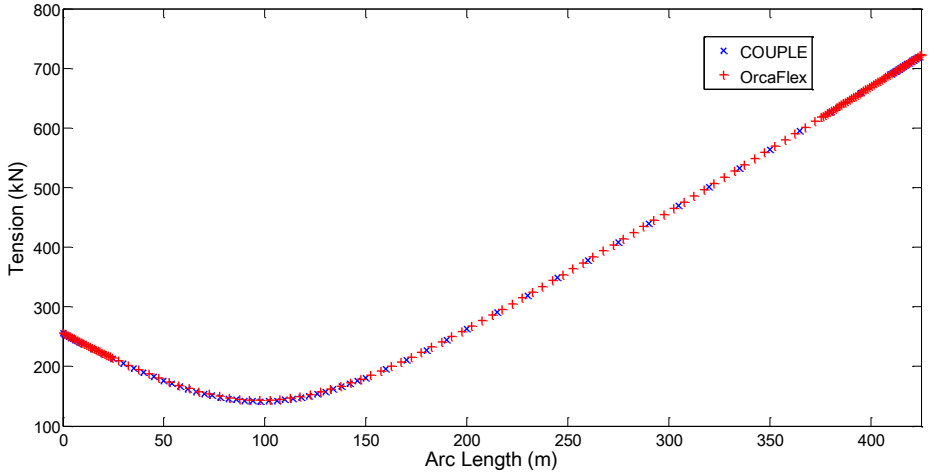

Figure 4.3 Tension along the flexible jumper of Case I

Figures 4.2 and 4.3 show the tension along the vertical riser and flexible jumper, respectively. The results calculated respectively using COUPLE and OrcaFlex are in satisfactory agreement. The arc length starts from the connection points of slender rods

at the URA. The tension along vertical riser is higher than flexible jumper due to the tension provided by the buoyancy can.

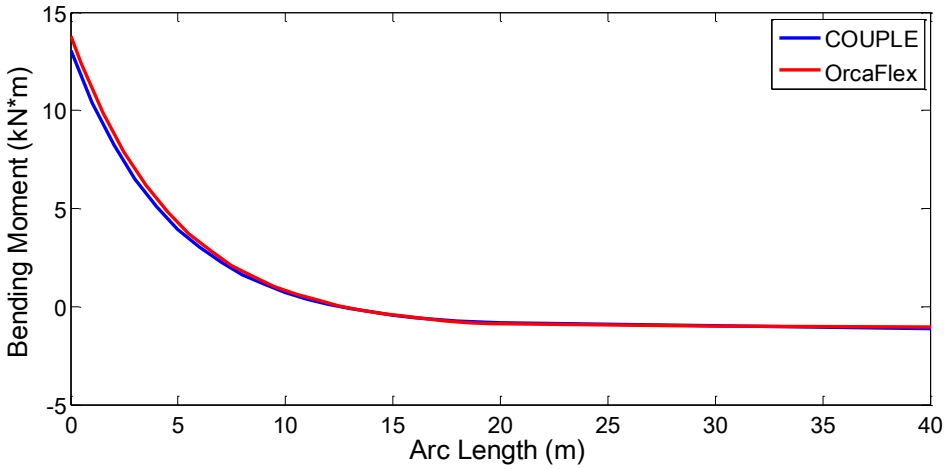

Figure 4.4 Bending moment along the vertical riser

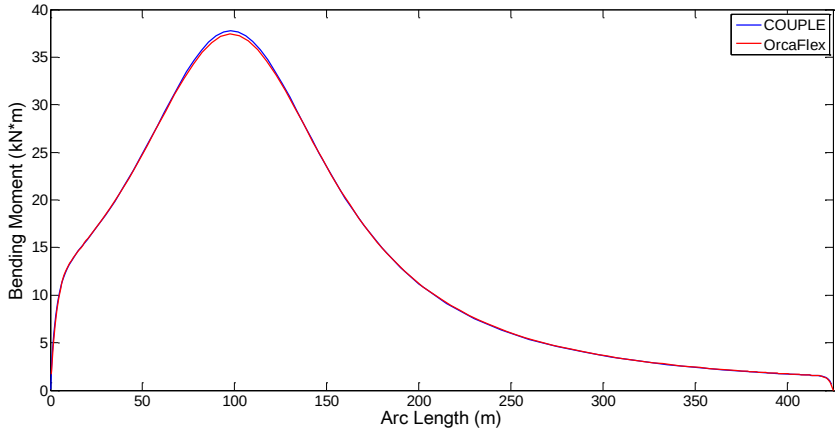

Figure 4.5 Bending moment along the flexible jumper of Case I

Figures 4.4 and 4.5 show the bending moment along the vertical riser and flexible jumper, respectively. Since the curvature at the mid-section of vertical riser reaches minimal, only the bending moment near the top connection is shown.

Table 4.2 Static loads from slender rods

	COUPLE	OrcaFlex
Tension at tether chain end on URA (kN)	5253.28	5251.27
Tension at vertical riser upper end (kN)	4825.89	4825.56
Tension at vertical riser lower end (kN)	2432.51	2447.41
Tension at flexible jumper upper end (kN)	722.50	722.69
Tension at flexible jumper lower end (kN)	256.3339	256.4046
Bending moment at vertical riser upper end (kN*m)	13.06	13.77
Bending moment at vertical riser lower end (kN*m)	105.68	104.72

Table 4.3 shows the comparison of static loads of slender rods calculated using COUPLE and OrcaFlex, respectively. Since the dimension of the URA is much smaller than a typical floater, the hydrodynamic force is insignificant. Therefore, the load of

slender rods is critical for the dynamic analysis of the URA. The comparison between the results obtained using COUPLE and OrcaFlex indicates satisfactory agreement.

4.1.2 Case II

The static results of Case II obtained using COUPLE are compared with those using OrcaFlex. It is noted that the static force applied by the flexible jumper is in the negative X-direction, the offset of the URA is also in the same direction. In Case I, one beam element is used to simulate the buoyancy can. The tether chain is discretized into 15 bar elements. The vertical riser is discretized into 141 beam elements. The flexible jumper is discretized into 88 beam elements.

Table 4.3 Static equilibrium position of the URA

	COUPLE		OrcaFlex	
	Without Flexible Jumper	With Flexible Jumper	Without Flexible Jumper	With Flexible Jumper
X (m)	0	-122.68	0	-122.58
Y (m)	0	0	0	0
Z (m)	-505	-506.85	-505	-506.26
Pitch Angle (degree)	0	-2.058	0	-2.057

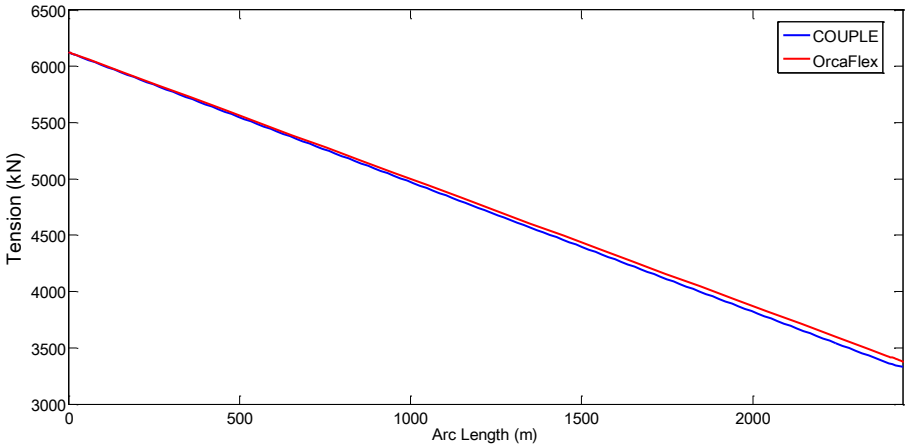

Figure 4.6 Tension along the vertical riser of Case II

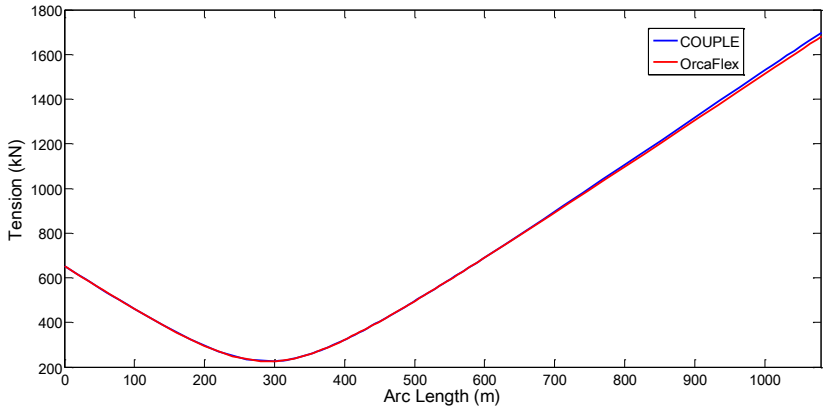

Figure 4.7 Tension along the flexible jumper of Case II

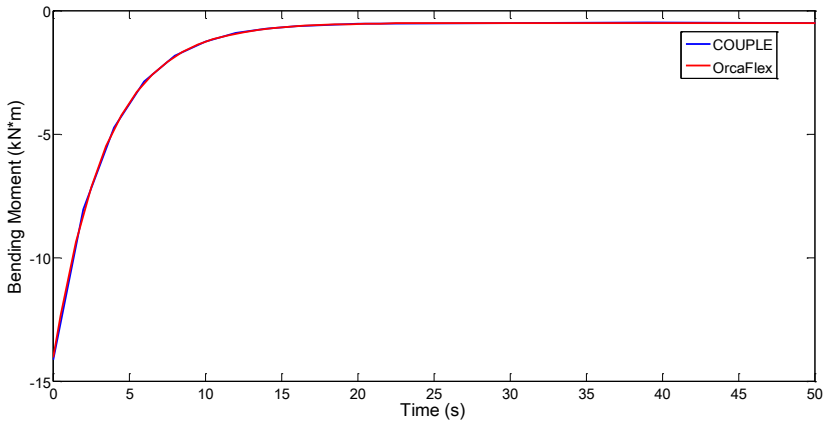

Figure 4.8 Bending moment near the vertical riser top end

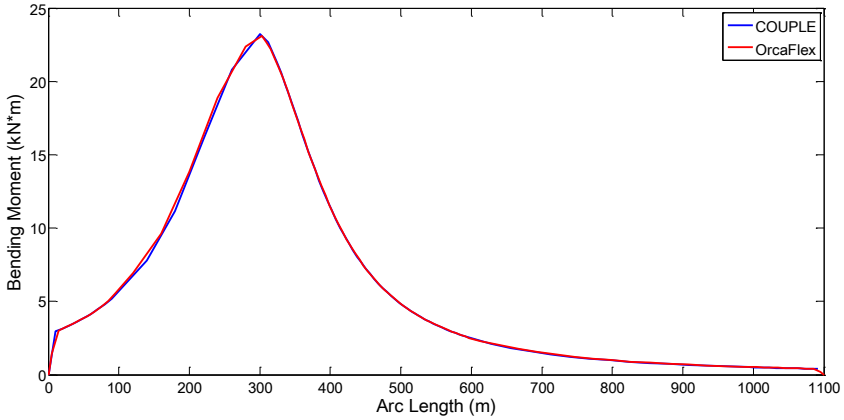

Figure 4.9 Bending moment along the flexible jumper of Case II

Table 4.4 Static loads from slender structures

	COUPLE	OrcaFlex
Tension at tether chain end on URA (kN)	6951.205	6951.21
Tension at vertical riser upper end (kN)	6127.624	6127.57
Tension at vertical riser lower end (kN)	3319.205	3319.37
Tension at flexible jumper upper end (kN)	721.85	720.97
Tension at flexible jumper lower end (kN)	652.54	652.57
Bending moment at vertical riser upper end (kN*m)	14.43	13.99
Bending moment at vertical riser lower end (kN*m)	120.36	114.05

Table 4.4 lists the static equilibrium position of the FSHR. Figures 4.6-4.9 show the tension and bending moment along the vertical riser and flexible jumper. The comparisons show satisfactory agreement between the results obtained using COUPLE and OrcaFlex.

4.2 Dynamic Simulations of FSHR due to the Vessel Oscillation

The dynamics of the FSHR is affected by three main sources: the motion of surface vessel connected to the jumper, vortex induced vibration (VIV) on the vertical riser and vortex induced motion (VIM) of the buoyancy can. The VIV on riser pipes is not included in this study. In this section, the dynamic response of the FSHR system to the vessel motions is investigated. It is assumed the vessel motion is not significantly affected by the force contributed from the jumper because the other loads on the vessel from the mooring line system and wind, wave and currents are much greater. Hence, the displacement at the flexible jumper hang-off point (connected to the vessel) is prescribed as a function of time according to the vessel motion and its relative location to the center of gravity of the vessel.

Because the URA is located about 150m below the water surface, the wave and wind loads directly applied on the FSHR are negligible, which are not considered in the simulation. On the other hand, wind and wave may dominate the motions of the surface vessel, such as FPSO and semi-submersible. Their effects on to the FSHR through

jumper are indirectly considered through the prescribed motion at hang-off point of the jumper.

4.2.1 Vessel Surge Motion

Typically, the natural period for horizontal (surge and sway) motion of a FPSO or Semi-submersible is greater than 100 seconds (DNV-RP-F205, 2010, Global Performance Analysis of Deepwater Floating Structures). The vessel horizontal motion induces the low frequency excitation for the FSHR system. For simplification, we assume the vessel surge motion is sinusoidal, the dynamic response of the FSHR system to the low frequency excitation is examined.

4.2.1.1 Case I

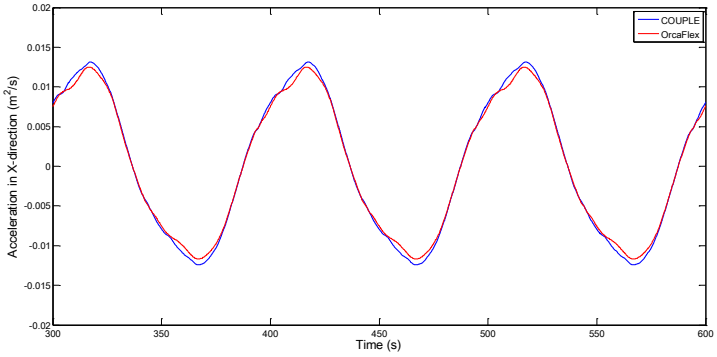

Figure 4.10 Acceleration of URA in X-direction

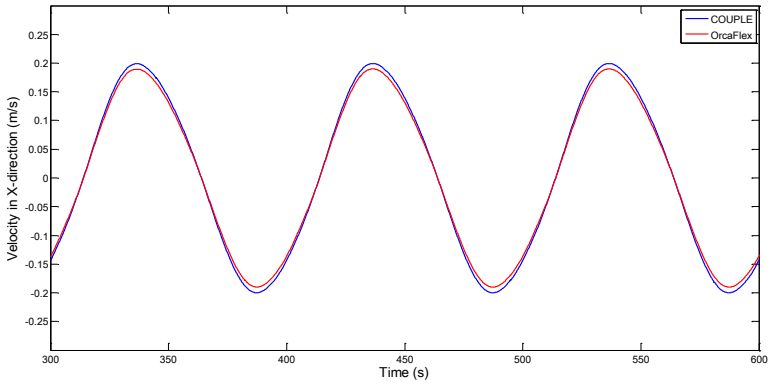

Figure 4.11 Velocity of URA in X-direction

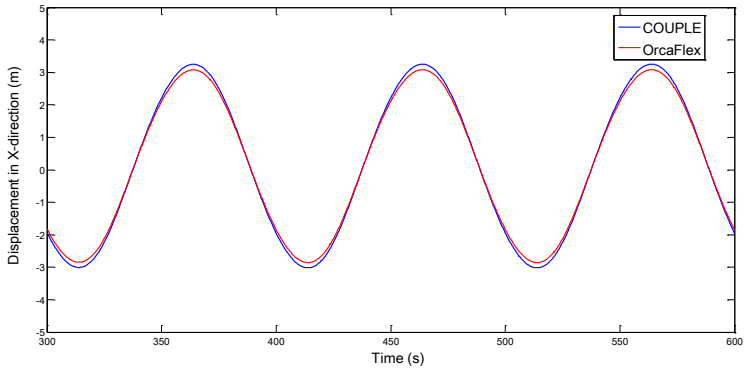

Figure 4.12 Displacement of URA in X-direction of Case I under surge motion

It is found convergence cannot be reached when the time step is set at 0.25s in the numerical simulation. On the other hand, the differences between the simulated results obtained, respectively, using the time step at 0.125s and 0.0625s are found to be negligible. Based on this convergence test, the time step 0.125s is used in all numerical simulation in this study.

Figures 4.10, 4.11 and 4.12 show the time series of the acceleration, velocity and displacement of the Upper Riser Assembly in X-direction in Case I. The vessel only has a sinusoidal surge motion. The amplitude of the surge is 10m and its period is 100s. It is noted that the displacement is plotted with the center of gravity of the URA when it is at the static equilibrium position. The results obtained respectively using COUPLE (blue line) and OrcaFlex (red line) match very well in both amplitude and period. Since the vertical riser top end is connected to the URA, the motion of the URA also reveals the dynamic characteristics of the vertical riser. The time series of the acceleration of the URA is insignificant. Comparing the surge amplitude of at hang-off point of the jumper to the amplitude of the URA, it is only 34.2% of the vessel surge motion is transferred to the vertical riser top, indicating the flexible jumper effectively insolates the motion of the surface vessel to the FSHR system.

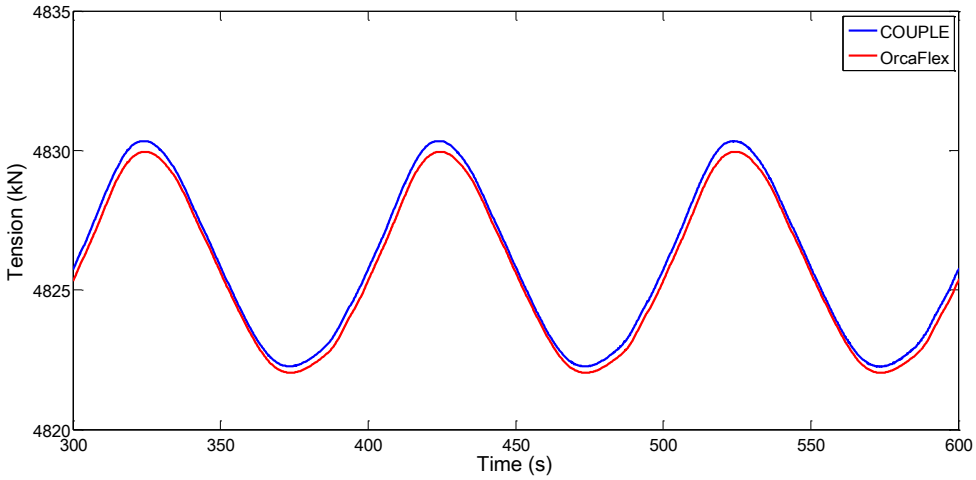

Figure 4.13 Tension on the vertical riser top end of Case I under surge motion

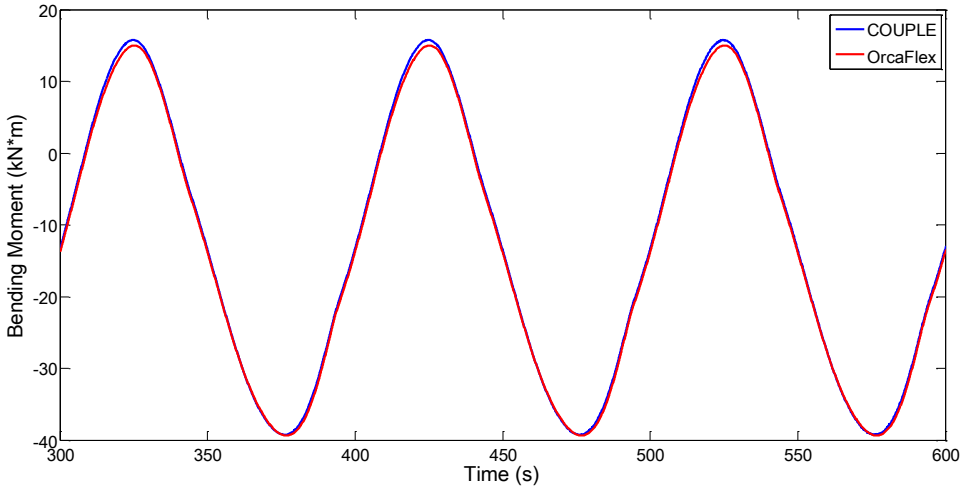

Figure 4.14 Bending moment on the vertical riser top end of Case I under surge motion

Figures 4.13 and 4.14 show the time series of the tension and bending moment at the top end of the vertical riser. The comparison in both figures shows that the results obtained using COUPLE and OrcaFlex is in satisfactory agreement. The dynamic tension variation is about 0.1% of the mean tension, indicating the tension induced stress variation is very small.

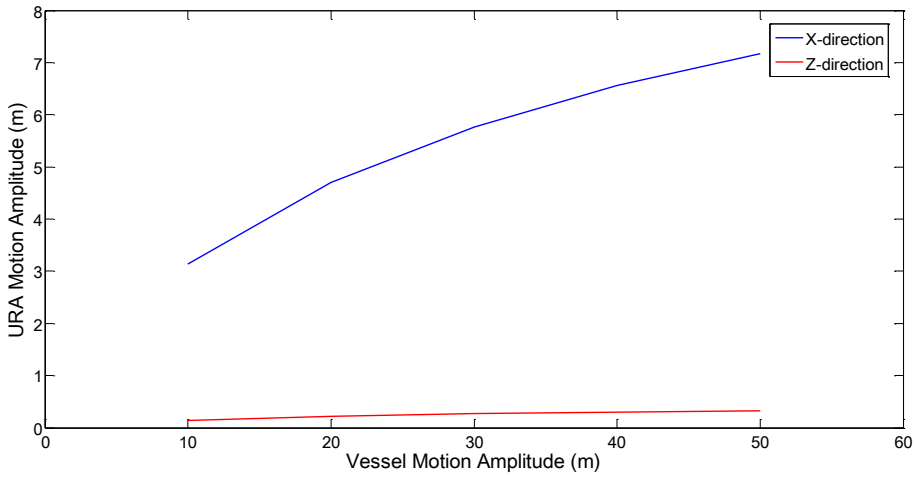

Figure 4.15 Displacement amplitude of URA of Case I under surge motion

Figure 4.15 plots the amplitude of the motion of the URA in the X-and Z-directions as a function of the surge amplitude of the hang-out point of the flexible jumper. For different surge amplitudes, the period of the surge motions remains the same, 100s. The results shown in Figure 4.15 indicate that the surge motion of the top end of the vertical riser is less than 35% of the vessel motion. Furthermore, the vertical motion of the riser top is negligible. These results verifies the advantage of the FSHR, that the motion of the vertical riser is “decoupled” from that of the vessel motion.

Table 4.5 Maximum tension, bending moment and stress of Case I

Vessel Motion Amplitude (m)	Maximum Tension (kN)			Maximum Bending Moment (kN*m)	Maximum Stress (kPa)
	Vertical Riser	Flexible Jumper	Tether Chain	Vertical Riser	Vertical Riser
10	4830.128678	262.6623	5253.402	39.79809	233846.3147
20	4834.997287	269.131	5253.485	60.22507216	241370.0291
30	4840.785935	275.2759	5253.524	89.19885977	253223.5847
40	4847.453986	280.7967	5253.558	118.7972141	264603.6445
50	4855.085478	285.4865	5253.587	146.6680163	275376.0381

Table 4.5 presents the maximum tension of different components at their connection with the URA and the maximum bending moment and stress applied at the vertical riser top. For the different surge amplitudes of the surface vessel, the surge period is the same, 100s. The maximum tension, bending moment and stress increase slightly with the vessel motion amplitude. However, the maximum tension in the tether chain does not change with the vessel motion amplitude. The uplift given by buoyancy virtually remains constant if the riser system is only excited by the vessel surge motion and VIM of the buoyancy can is not considered. The dynamic response of the riser system is not sensitive to the low frequency motion amplitude.

4.2.1.2 Case II

The dynamic response of the FSHR of Case II under the vessel surge motion excitation is examined. The vessel surge motion is sinusoidal with the amplitude 50m and period 100s.

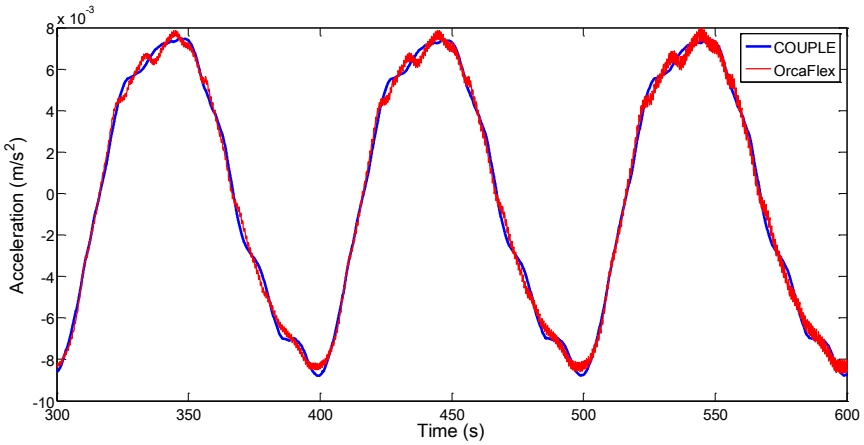

Figure 4.16 Acceleration of the URA

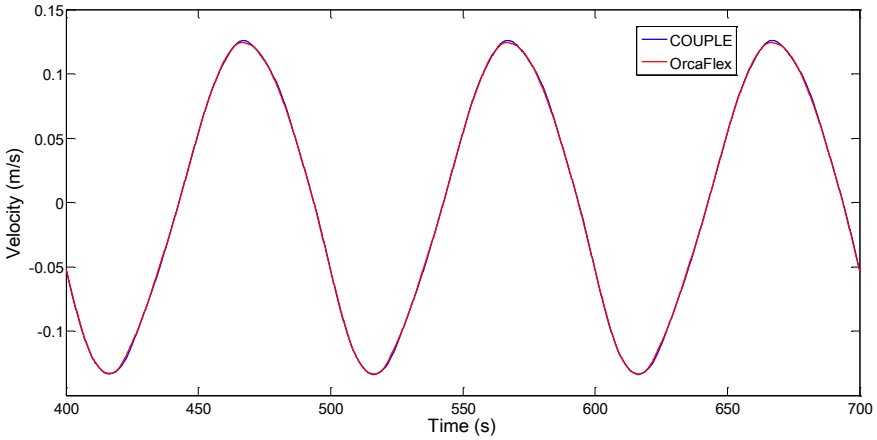

Figure 4.17 Velocity of the URA

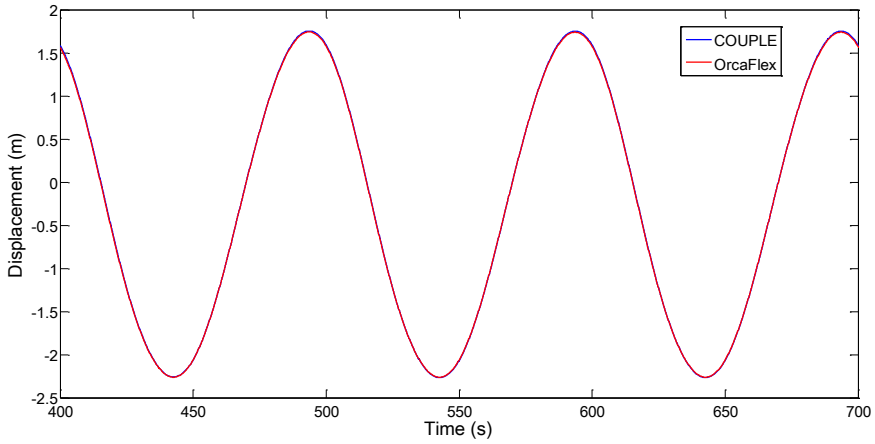

Figure 4.18 Displacement of the URA

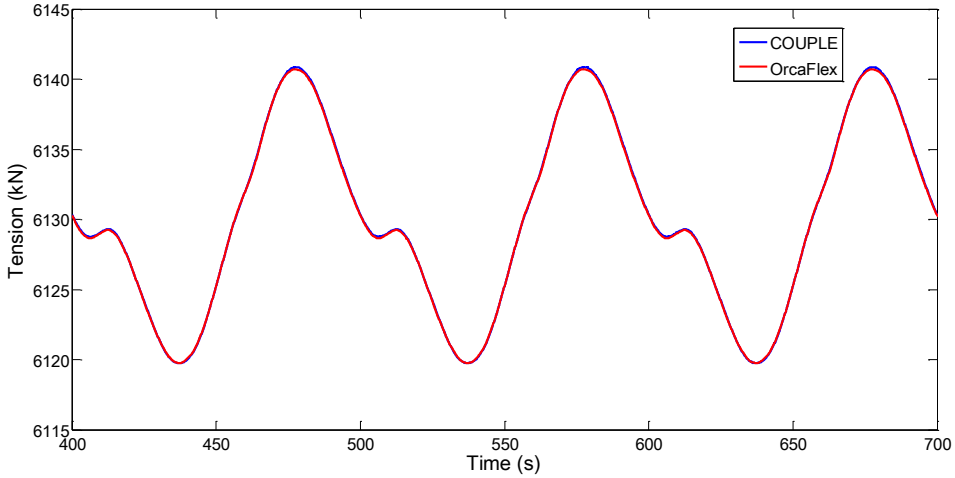

Figure 4.19 Tension at the vertical riser top end of Case II under vessel surge motion

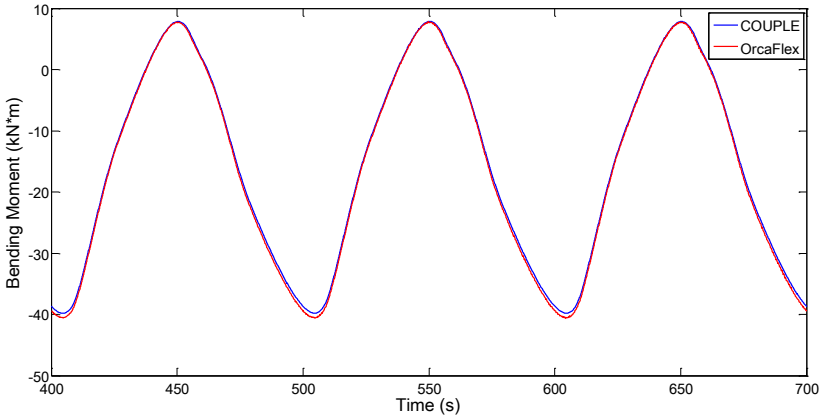

Figure 4.20 Bending moment at the vertical riser top end of Case II under surge motion

Figures 4.16-4.18 plot the simulated acceleration, velocity and displacement of the URA in the X-direction as a function of time. Figures 4.19 and 4.20 present the tension and bending moment at the top end of the vertical riser. The comparison between the results respectively simulated using COUPLE and OrcaFlex is in satisfactory agreement, except for the acceleration simulated using OrcaFlex has high-frequency noises at the peak and trough.

4.2.2 Vessel Heave Motion

For floaters, such as the FPSO and Semi-Submersible, the natural period of their heave motion is typically at the ocean wave period range, from 5s to 30s (DNV-RP-F205, 2010, Global Performance Analysis of Deepwater Floating Structures). Therefore, we investigate the vessel heave motion at the wave frequency that excites the FSHR.

4.2.2.1 Case I

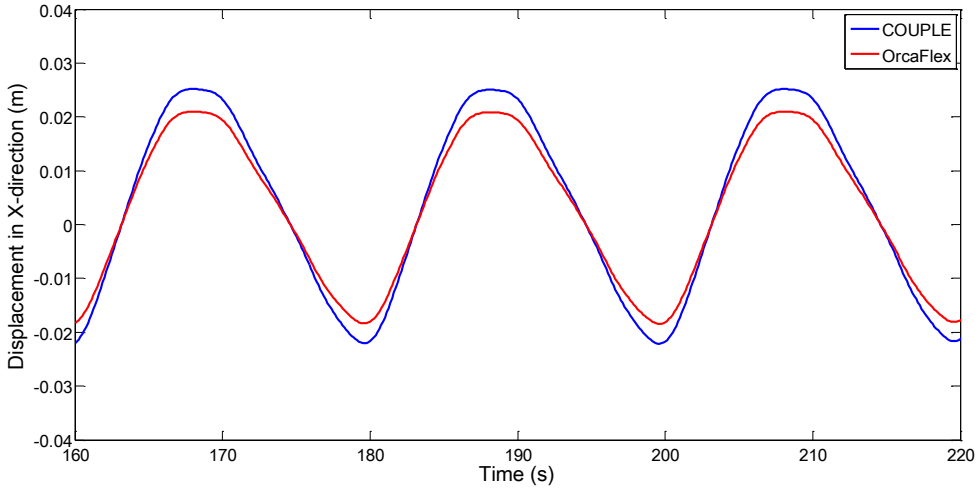

Figure 4.21 Displacement of URA in X-direction of Case I under heave motion

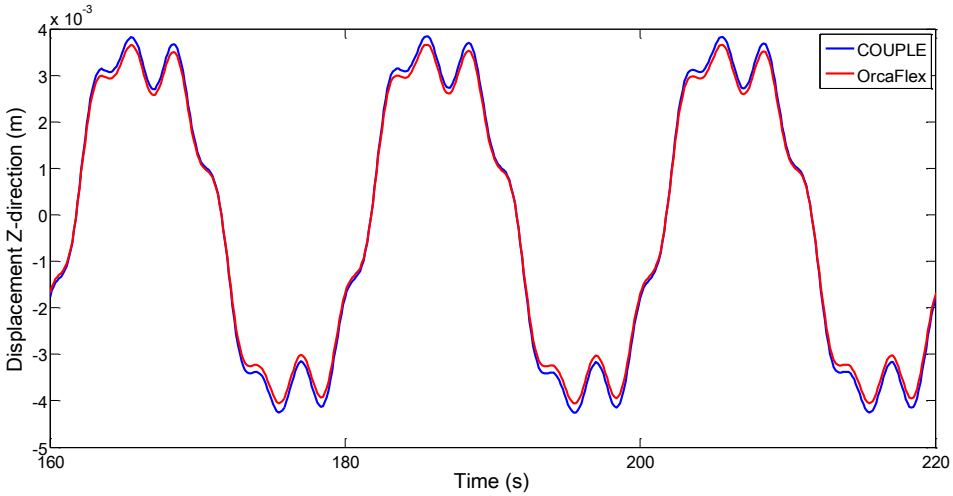

Figure 4.22 Displacement of URA in Z-direction

Figures 4.21 and 4.22 present the time series of the displacement of the URA in the X- and Z- direction, respectively. The vessel heave motion is sinusoidal with the amplitude 4m and period 20s. The motion of the URA is less than 1% of vessel heave motion in terms of the amplitude.

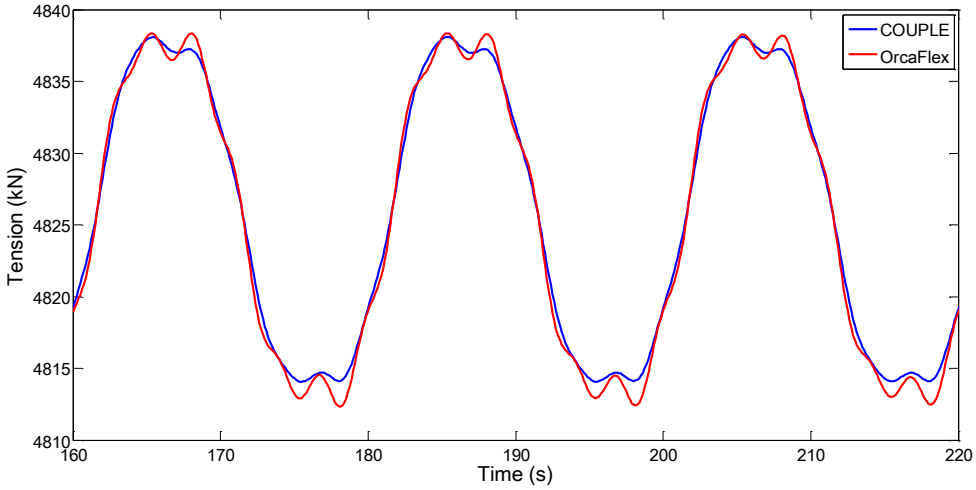

Figure 4.23 Tension at vertical riser top end of Case I under vessel heave motion

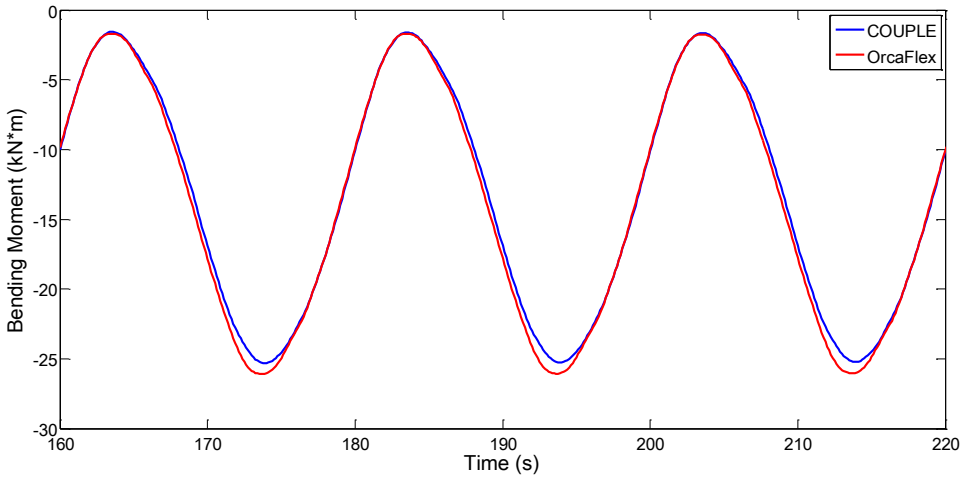

Figure 4.24 Bending moment at vertical riser top end of Case I under vessel heave motion

Figures 4.23 and 4.24 show the time series of the tension and bending moment at the top end of the vertical riser. As shown in Figures 4.21-4.24, the agreement between the two results obtained using the codes respectively remains satisfactory. Although the

motion at the top vertical riser is insignificant, the amplitude of tension variation is larger than that induced by the vessel surge motion.

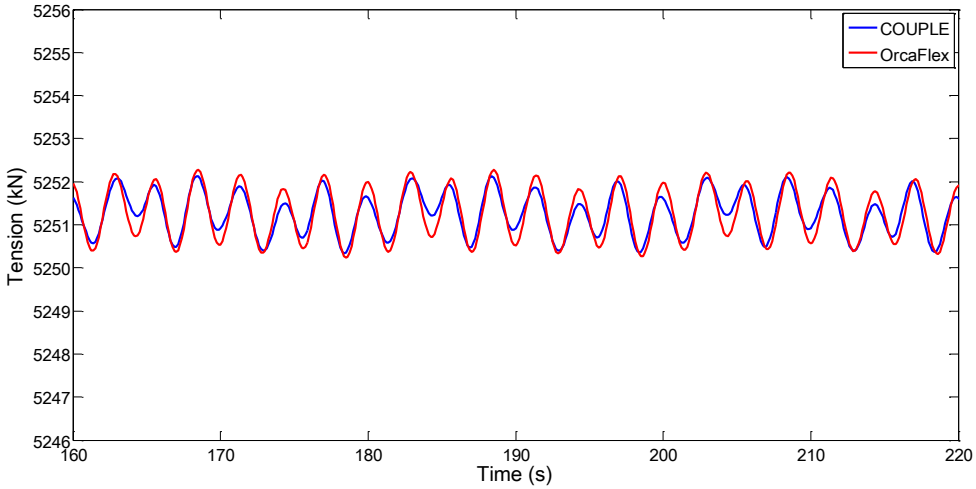

Figure 4.25 Tension in tether chain

Figure 4.25 shows the time series of the tension in tether chain which represents the uplift force given by the buoyancy can. It shows the frequency of the tension is about 7 times of the vessel heave frequency. It has been shown that the high frequency indeed matches the heave natural frequency of the FSHR in the absence of the flexible jumper. This phenomenon is crucial to the fatigue damage in the tether chain.

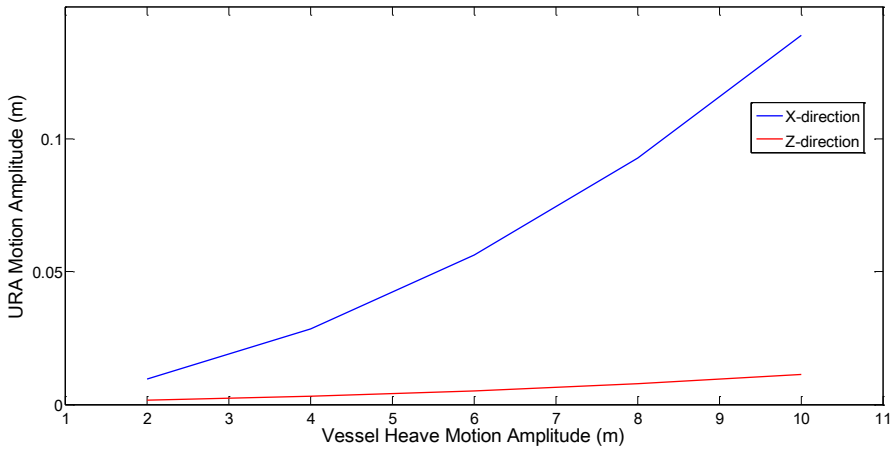

Figure 4.26 Displacement amplitude of URA of Case I under heave motion

Figure 4.26 shows the URA motion amplitude versus the vessel heave motion amplitude. For all amplitudes of the vessel heave motions considered in our simulation, the heave period remains the same, 20s. The results show that the motion of the vertical riser top is insignificant due to the heave excitation induced by the surface vessel. This characteristic of the FSHR is quite different from the SCR of which the fatigue damage at the touch down zone is sensitive to the vessel heave motion.

Table 4.6 Maximum tension, bending moment and stress

Vessel Motion Amplitude (m)	Maximum Tension (kN)			Maximum Bending Moment (kN*m)	Maximum Stress (kPa)
	Vertical Riser	Flexible Jumper	Tether Chain	Vertical Riser	Vertical Riser
2	4831.989	260.8329	5252.384	14.83796	225968.6182
4	4838.29	268.3087	5252.669	25.5125	230322.1331
6	4846.479	280.1118	5253.04	37.4973	235299.9268
8	4858.27	296.2241	5253.435	50.65274	240825.7152
10	4872.771	316.6667	5253.8	65.13316	246969.017

Table 4.6 lists the maximum tension of different components at their connection to the URA and the maximum bending moment and stress on the vertical riser top. The maximum value of these variables does not increase with vessel heave motion amplitude significantly. Despite the minimal riser top motion, the variations of tension and bending moment are more significant than those induced by low frequency surge excitation.

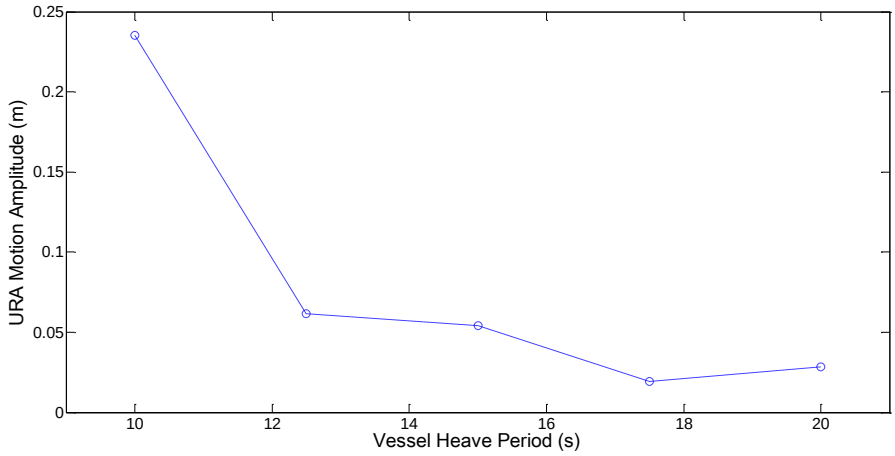

Figure 4.27 URA motion amplitude in X-direction

Figure 4.27 presents the motion amplitude of the URA versus the vessel heave motion period. For the simulations given in this figure, the vessel heave motions have the same amplitude at 4m. It shows that the URA motion amplitude reduces with the increase in the heave motion period. The higher the frequency vessel motion is, the larger motion of the riser system has.

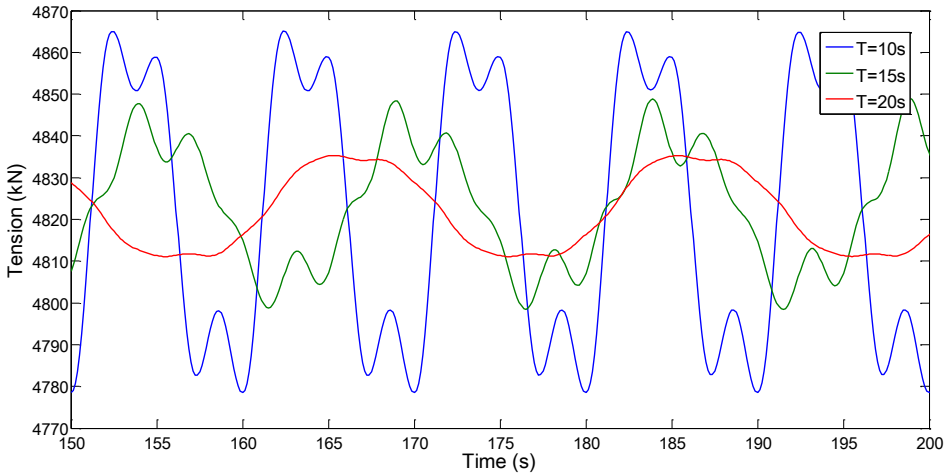

Figure 4.28 Tension at vertical riser top end with different vessel heave periods

Figure 4.28 shows the tension at the top of the vertical riser as a function of time induced by the vessel heave motions with different periods. The amplitude of the tension variation reduces with the increase in the periods of vessel heave motion. It is also observed that higher harmonics occur in the variation of tension in the case of higher frequency heave motion.

4.2.2.2 Case II

The results of the response of the FSHR of Case II to the excitation of the vessel heave motion are reported in this section. Similar with the Case I, the vessel heave motion is assumed to be sinusoidal with amplitude 4m and period 20s. Similar to the related results shown in Case I, the motion of the URA is found to be insignificant. Therefore, only the comparisons of tension, bending moment and stress at the top of the vertical riser simulated respectively using COUPLE and OrcaFlex are presented.

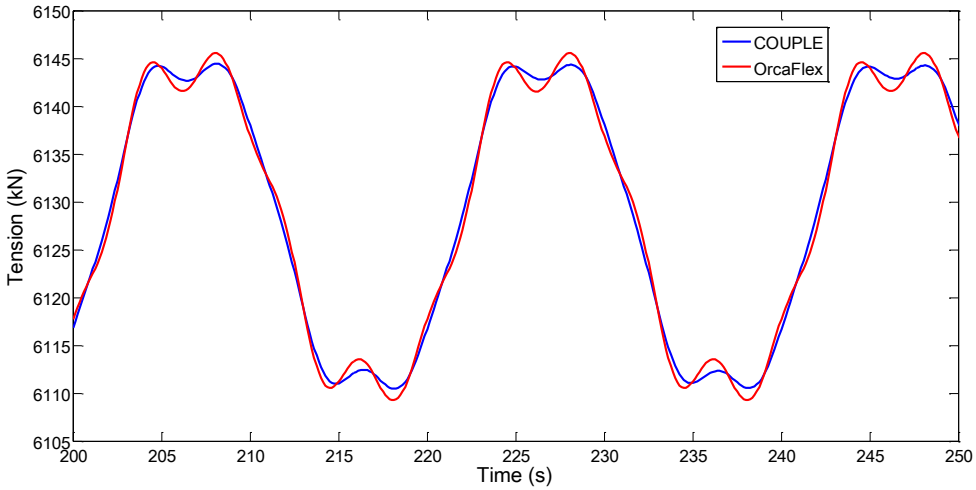

Figure 4.29 Tension at vertical riser top end of Case II under vessel heave motion

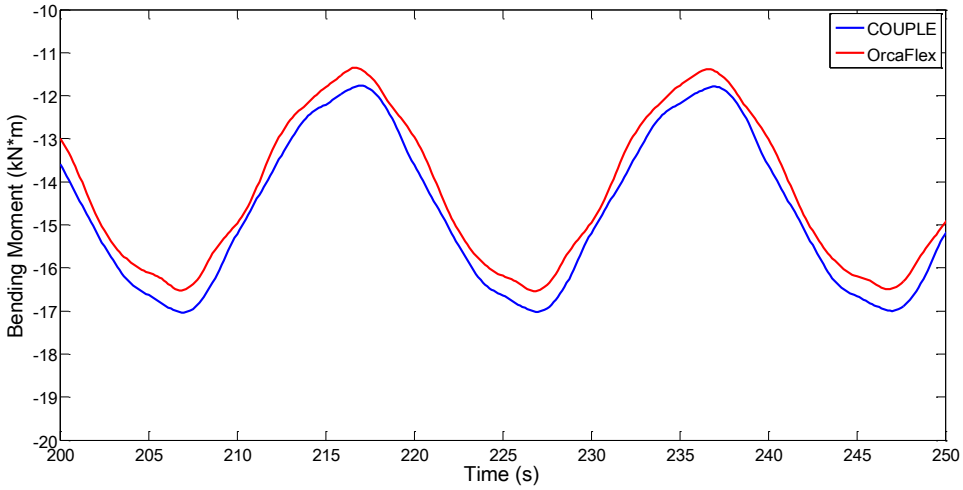

Figure 4.30 Bending moment at vertical riser top end of Case II under vessel heave motion

Figures 4.29 and 4.30 show the time series of the tension and bending moment at the top end of the vertical riser. The simulated tensions and bending moments respectively using COUPLE and OrcaFlex are in satisfactory agreement.

Since the vessel surge and heave motion is the in-line excitation to the FSHR, M_x found to be zero and the maximum stress variation occurs at β=0 degree.

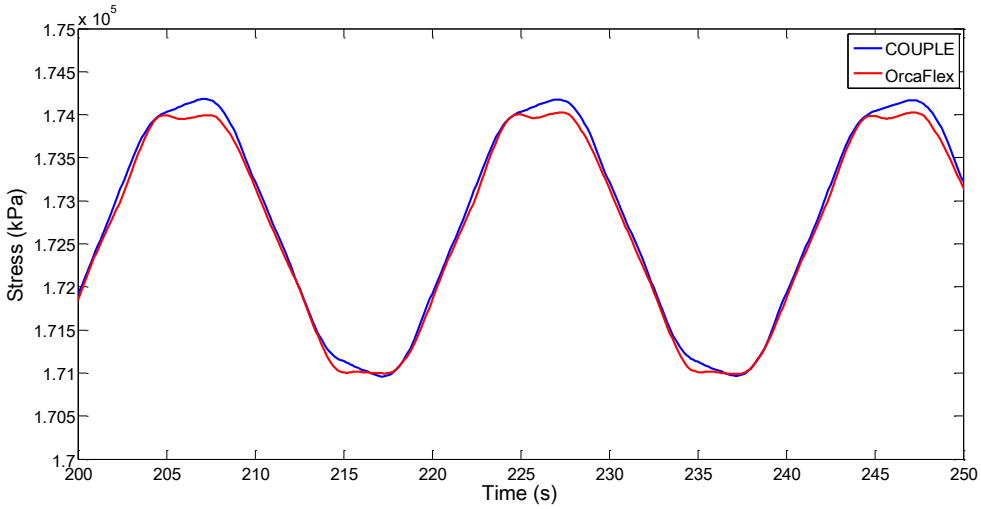

Figure 4.31 Stress at vertical riser top end of Case II under vessel heave motion

Figure 4.31 presents the time series of the stress (at β=0) at the top of the vertical riser. The results simulated, respectively, using the two codes are close.

4.2.3 Fatigue Damage Estimation of the Vertical Riser

In reality, the surface vessel is excited by irregular waves and experiences 6 DOF (degree of freedom) motions. The displacement at the hang-off end of the flexible jumper as a function of time depends on the motion of the vessel and its location with respect to the center of gravity of the vessel. The displacement at the hang-off end of the jumper is in general of three-dimensional (surge, sway and heave) and irregular. Therefore, for the purposes of studying the fatigue damage of the vertical riser, the dynamic response of a FSHR under irregular excitation is investigated.

In this study, the surface vessel under the impact of irregular ocean waves is a FPSO. Irregular waves considered in the simulation are assumed to follow a JONSWAP spectrum with a sharp factor of 6. The wave scatter diagram is provided by Chang *et al* (2012). For simplicity, the wave condition is reduced into 4 bins from the original 12 bins. It should be noted that the estimated fatigue damage based on the simplified wave condition is likely more conservative because the probability of the bin of larger wave height is higher than the original one. The wave direction is assumed to be 0 degree in the global coordinate system. The numerical simulation of the FSHR of Case I is made for 3 hours under each wave condition. The significant wave height, peak period, and probability of each wave condition are listed in Table 4.7.

Table 4.7 Wave scatter diagram for fatigue analysis

Hs (m)	Tp (s)	Probability (%)
0.4	11.9	35.25
1.01	13.3	46.95
1.31	14.6	2.32
2.29	16	15.48

The motion of the vessel is calculated based on the motion RAO. The JONSWAP spectrum is firstly decomposed into individual wave components. Then, the 6-DOF motion of the vessel at each time step can be obtained using equation (4.1).

$$x(t) = \sum A_i a_i \cos(\omega_i t + \varphi_i + \psi_i) \tag{4.1}$$

A_i (m/m) is the motion RAO amplitude at the wave frequency ω_i,

a_i (m) is the amplitude of the wave component at the wave frequency ω_i,

φ_i (rad) is the random phase of the wave component at the wave frequency ω_i,

ψ_i (rad) is the phase of the motion RAO at the wave frequency ω_i.

The length of the surface vessel (FPSO) is 320.04 m. The mass of the FPSO is 309800 ton. The origin of the body-fixed coordinate system of the vessel is located at the center of gravity of the FPSO. The coordinates of the hang-off point in the body-fixed coordinate system of the vessel are (-160m, 0, 0). The motion RAO of the FPSO is provided by Chang (2014). Detailed motion of RAO of the FPSO is presented in Appendix II.

The displacement of the hang-off point of the flexible jumper as a function of time is then calculated based on the translational and rotational motion of the vessel and the location with respect to the center of gravity of the vessel. The displacement as a function of time is the input, which describes the excitation at the upper end of the flexible jumper. In this way, the tension and bending moment at the top of the vertical riser induced by the irregular vessel motion can be simulated.

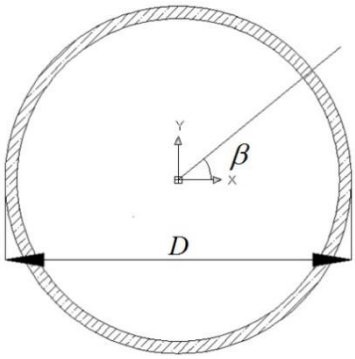

Figure 4.32 Vertical riser pipe cross section

Knowing the tension and bending moment of the vertical riser, the related stress around the riser outer circumference, is assessed by equation (4.1). The x and y-axis in the riser top cross section plane is parallel to the body-fixed coordinate system of the rigid body. The x-direction is defined as the in-line direction and the y-direction the cross-flow direction, as shown in Figure 4.32.

$$\sigma = \frac{T}{A} + \frac{D}{2}\left(\frac{M_x}{I_x}\sin\beta - \frac{M_y}{I_y}\cos\beta\right) \tag{4.2}$$

In equation (4.2),

σ is the axial stress which is the combination of tensile stress and bending stress,

T is the tension assumed to be uniformly distributed across the stress area,

A is the cross section area,

D is the outer diameter,

M_x and M_y are the bending moment with respect to x and y-axis,

I_x and I_y are the moment of inertia with respect to x and y-axis,

β is the angle defined in Figure 4.32.

The S-N curve is often used for assessing the fatigue damage. In this study, the fatigue damage at the top of the vertical riser is estimated using DNV S-N B1 curve (seawater with cathodic protection, DNV RP-C203, 2010, Fatigue Design of Offshore Steel Structures), which applies to steel riser material. The fatigue damage is calculated using equations (4.3) and (4.4).

$$S^m N = a \tag{4.3}$$

where *S* is the stress range (MPa);

N is the cyclic number of fatigue life allowed within the stress range *S*.

a and *m* are the parameters defining the curves. In this study, $m = 3.0$ and $\log\ a = 12.513$.

$$Fatigue\ Damage = \sum \frac{n_i}{N_i} \tag{4.4}$$

n is the cyclic number under the corresponding stress range during the design life span of the FSHR;

N is the allowable cyclic number under the corresponding stress determined by equation (4.3). The rainflow-counting algorithm is used to count cycle numbers for the given stress range.

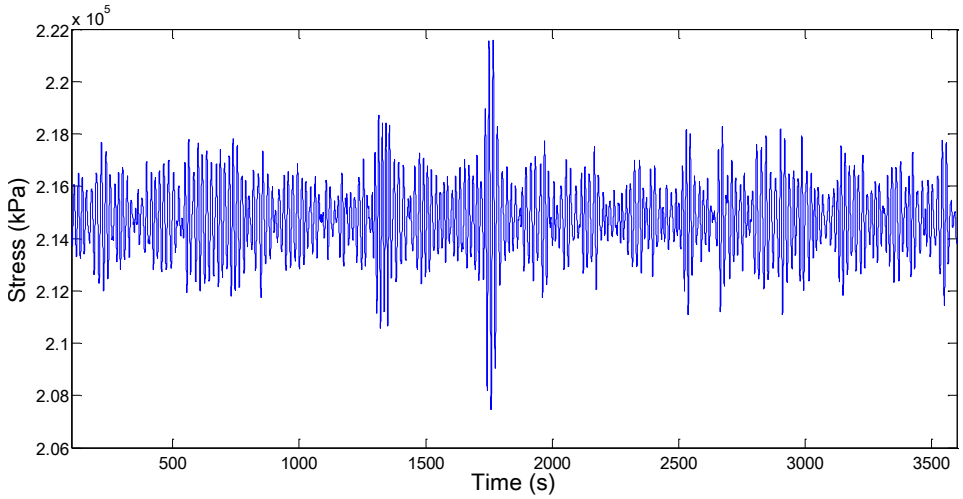

Figure 4.33 Stress at the vertical riser top end under irregular wave conditions

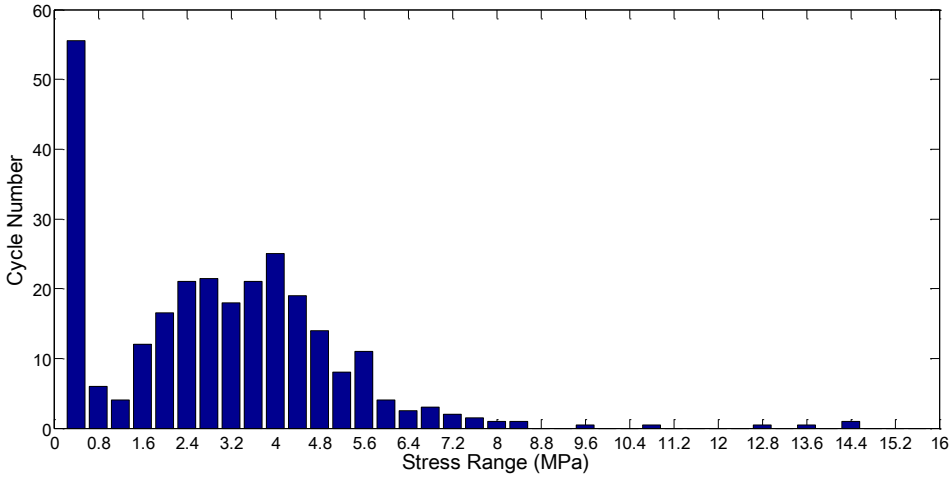

Figure 4.34 Stress histogram

Figure 4.33 presents the three-hour time series of stress at the top end of the vertical riser at β=0 degree. Figure 4.34 is the stress histogram given by the rainflow-counting technique based on the stress time series shown in Figure 4.33.

Table 4.8 Fatigue damage

Hs (m)	Tp (s)	Probability (%)	Fatigue damage in 3 Hour	Possible Fatigue damage in 3 Hour	Possible Fatigue damage in 1 Year
0.4	11.9	35.25	2.45482E-10	8.65326E-11	2.52675E-07
1.01	13.3	46.95	7.10137E-10	3.33409E-10	9.73556E-07
1.31	14.6	2.32	1.86613E-09	4.32943E-11	1.26419E-07
2.29	16	15.48	1.99672E-08	3.09092E-09	9.02549E-06

Table 4.8 lists the fatigue damages for the four wave conditions. The summation of the fatigue damage in each wave condition is the expected total fatigue damage in one year. It is found to be 1.03781×10^{-5}. So, the fatigue life is 1 divided by the fatigue damage, 96356 years. This high fatigue life indicates the vessel motion induced fatigue damage to the FSHR is not insignificant. This is why the design concept of the FSHR was envisioned.

4.3 Dynamic Simulations of FSHR due to Buoyancy Can VIM

It is known that currents passing the cylindrical buoyancy can causes vortex shedding, which in turn produces oscillating lift force on the can. The magnitude of the oscillating lift force is approximated by an empirical formula shown in equation (4.5). The direction of the oscillating lift force is assumed to be perpendicular to the current direction. The current velocity considered in this study ranges from 0.22m/s to 1.44m/s.

$$\left|\vec{q}_{VIM}(t)\right| = \frac{1}{2}\rho_f D C_L U_c^2 \sin(2\pi f_s t) \tag{4.5}$$

where,

$\vec{q}_{VIM}$ is the force per unit length due to vortex shedding from the buoyancy can,

ρ_f is the ambient fluid density,

D is the diameter of the buoyancy can,

C_L is the lift force coefficient,

U_c is the current speed,

f_s is the vortex shedding frequency,

In using equation (4.5), the vortex shedding frequency and lift force coefficient need to be determined in advance. The following analysis is only performed for the FSHR of Case I.

4.3.1 Natural Frequency

The natural frequency of the FSHR system is determined by the free decay test. During the test, the riser system is firstly excited by a sinusoidal motion at the flexible jumper hang-off point in the surge or sway direction. After 500 seconds, the excitation suddenly stops. The riser system will continue vibrating and the amplitude of the oscillation decays due to the viscous damping.

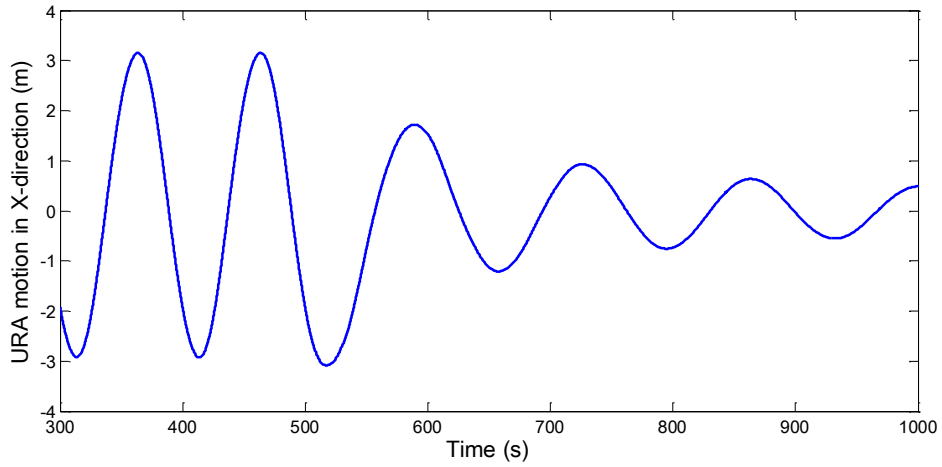

Figure 4.35 Time series of URA motion in X-direction

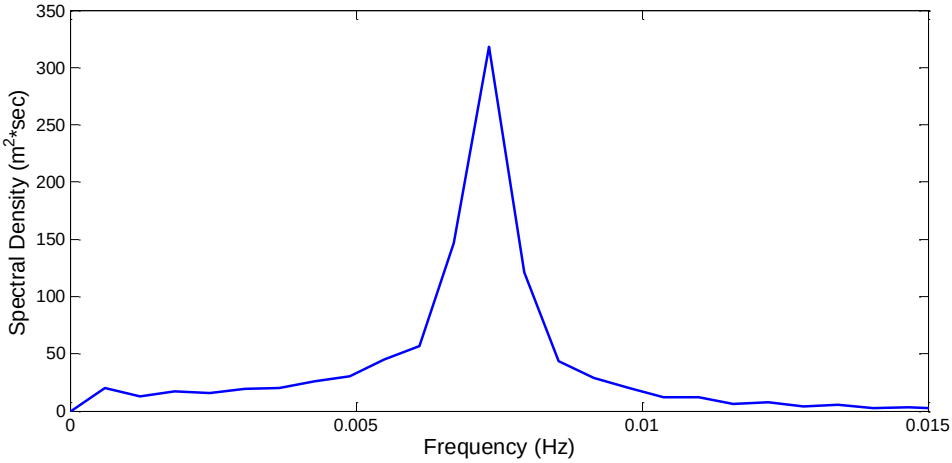

Figure 4.36 Spectrum of URA motion in X-direction in free decay stage

The decay test is firstly done in the X-direction. Figure 4.35 shows the time series of the URA motion, and the related power density spectrum is given in Figure 4.36. It is noted that the first 500-second time series is excluded in deriving the power

spectrum. Figure 4.36 shows the peak frequency is at 0.007324Hz. Hence, the natural period of the riser system in the X-direction is about 136.53 seconds.

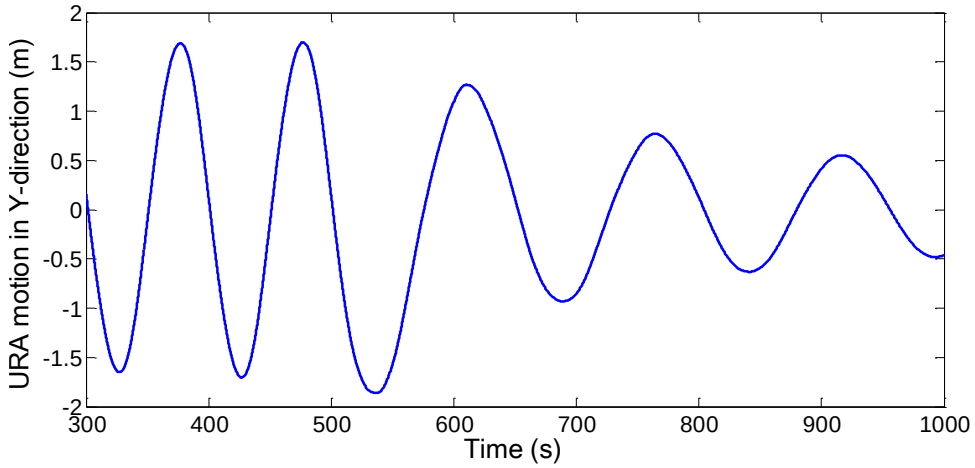

Figure 4.37 Time series of URA motion in Y-direction

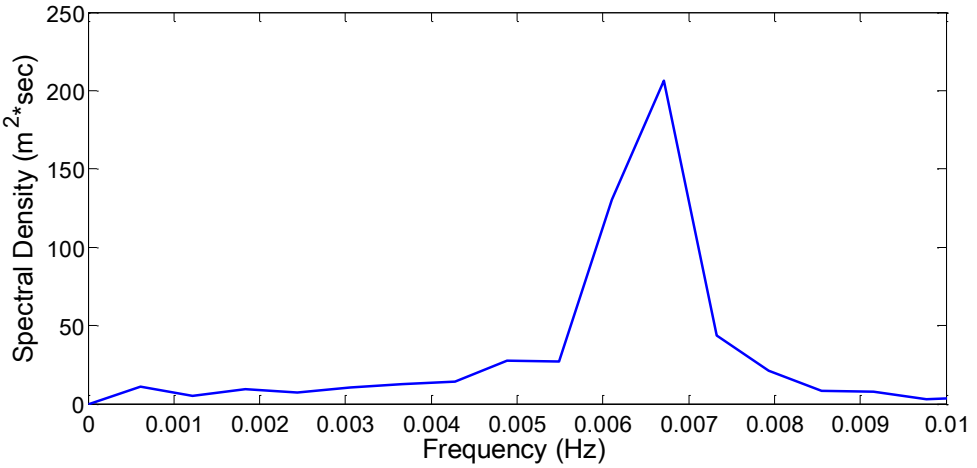

Figure 4.38 Spectrum of URA motion in Y-direction in free decay stage

Similarly, the free decay test is performed in the Y-direction. Figure 4.38 shows the peak frequency is at 0.006714Hz, and thus the natural period of the riser system in

the Y-direction is about 148.94 seconds. The natural period of the riser system in the Y-direction is longer than that in the X-direction, which means the stiffness of the system in the Y-direction is smaller. Therefore, the analysis is performed for the current coming from the X-direction, which induces the motion of buoyancy can in the cross-flow direction (Y-direction).

4.3.2 Vortex Shedding Frequency

The lift force coefficient and vortex shedding frequency for the simulating the VIM of the buoyancy can are determined based on the experiment results by Pereira *et al* (2005). In their experiments, two different scales of models (1:50 and 1:100) were tested. The experimental data of the 1:50 model test were used in this study. The oscillation of the buoyancy can was measured under different current speeds. The current direction is parallel to the flexible jumper plane (the X-direction).

The definitions of the reduced velocity and Strouhal number are given below.

$$V_r = \frac{U_c}{f_n D} \tag{4.6}$$

V_r is known as the reduced velocity, which is non-dimensional,

U_c is the current speed,

f_n is the natural frequency of the FSHR system,

D is the diameter of the buoyancy can.

$$St = \frac{f_s D}{U_c} \tag{4.7}$$

St is the Strouhal number,

f_s is the vortex shedding frequency.

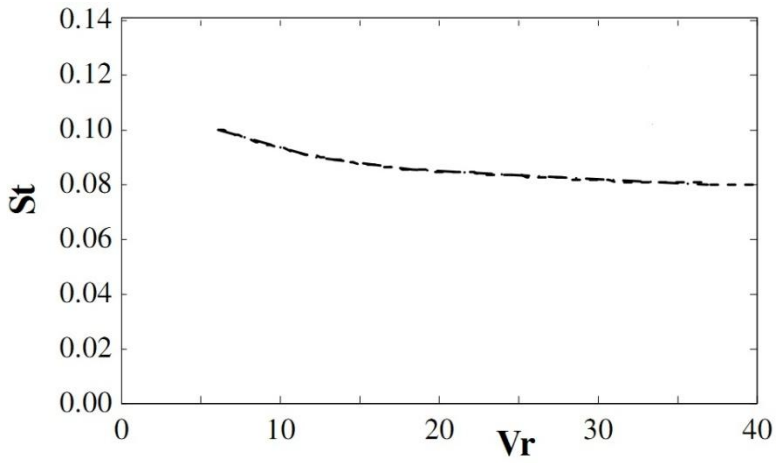

Figure 4.39 Strouhal number (St) from transverse buoyancy can oscillation versus reduced velocity (Vr)

Figure 4.39 presents the Strouhal number versus reduced velocity, where vortex shedding frequency is assumed to be the same of that of the buoyancy can oscillation measured in the experiment (Pereira *et al*, 2005). The experimental data showed that the Strouhal number is less than 0.2. The latter was based on the experiments of fixed long cylinder. This could be explained by tridimensional flow effects around the buoyancy can which has a small aspect ratio (*L/D*) (Pantazopoulos, 1994).

4.3.3 Lift Force Coefficient

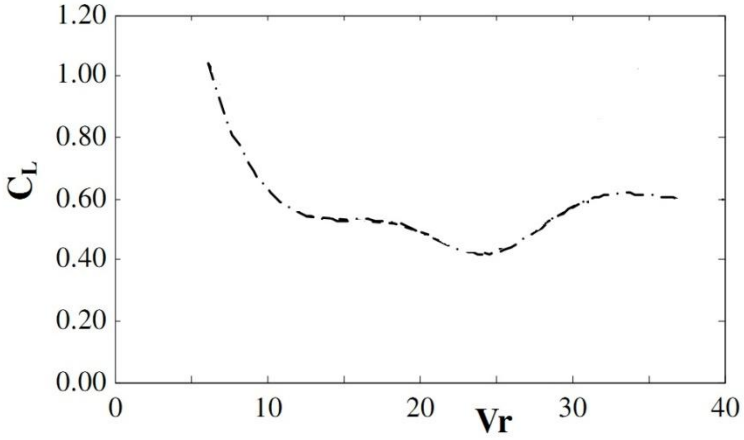

Figure 4.40 Lift coefficient versus reduced velocity

The lift coefficient was implicitly determined based on the results of the experiment. Several simulations has been systematically made using different lift coefficients. The final lift coefficient was chosen such that the difference between the simulated and measured *A/D* is less than 5 %, where A is the amplitude of VIM of the buoyancy can (Celso, 2012).

4.3.4 Amplitude of the VIM of the Buoyancy Can

Table 4.9 Parameters for buoyancy can VIM simulation

Reduced Velocity	Current Speed (m/s)	Strouhal Number (From Experimental Curve)	Lift Force Coefficient (From Experimental Curve)	Vortex Shedding Period (s)
6	0.219543457	0.09989324	1.044128	248.5077
9	0.329315186	0.09516014	0.6939502	173.912
12	0.439086914	0.09	0.5530249	137.9125
15	0.548858643	0.08768683	0.5252669	113.2405
20.4	0.746447754	0.08419929	0.4932384	86.71389
25	0.914764404	0.08245552	0.424911	72.25493
30	1.097717285	0.08145907	0.572242	60.949
39.3	1.438009644	0.07871886	0.6	48.14552

Table 4.9 lists the lift coefficients and vortex shedding periods, which were read from the experimental curves, under different current speeds. These parameters were used to simulate the VIM of the buoyancy can in our study.

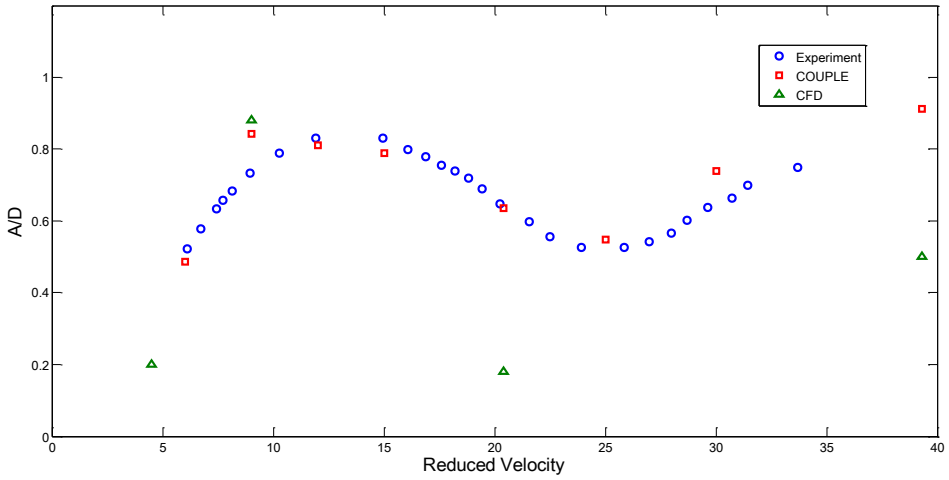

Figure 4.41 Non-dimensional oscillation amplitude (A/D) versus reduced velocity

Figure 4.41 compares the simulated and measured non-dimensional oscillation amplitude as function of the reduced velocity. The red squares are simulated using COUPLE, the green triangle by CFD (Minguez, 2011) the blue circles are experimental data (Celso, 2012). The results of COUPLE matched very well with the experimental data in the range of low reduced velocity (Vr<20). For higher reduced velocities, the non-dimensional oscillation amplitude given by COUPEL is slightly greater than the experiment data. However, the results from the CFD are much smaller than those of COUPLE and experiment. This indicates that, by utilizing the Strouhal numbers and lift coefficients given by the experiment, COUPLE may accurately reproduce the VIM of the buoyancy can.

4.3.5 Stress at the Vertical Riser Top

The stresses at the top end of the vertical riser are simulated and processed for the various angles of β=0, 45, 90, 135, 180, 225, 270 and 315 degree. β=0 and 180 degree indicate the in-line direction, and β=90 and 270 degree indicate the cross-flow direction. Since the VIM of buoyancy can is modeled as a sinusoidal motion, the stress variation is also periodic when the FSHR system is only excited by the buoyancy can‟s VIM. The time series of stress shows it is periodic.

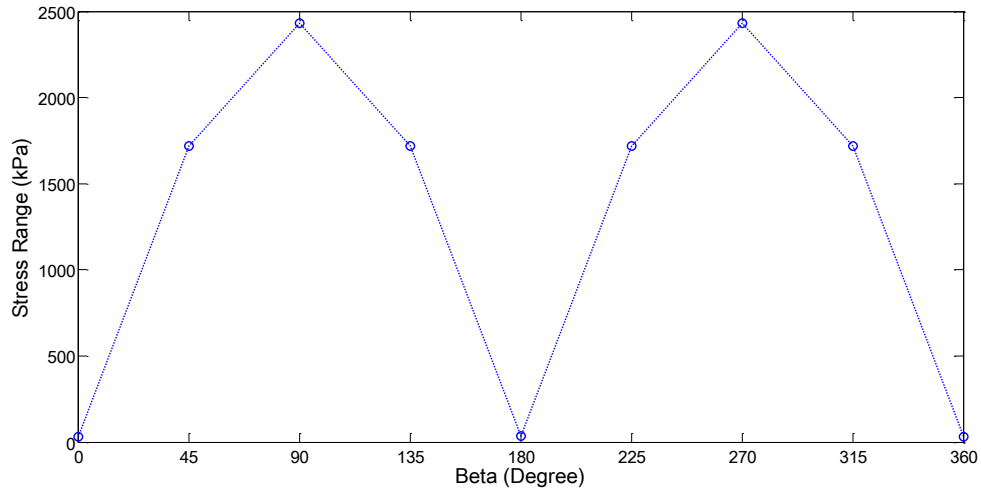

Figure 4.42 Stress range around the riser circumference

Figure 4.42 shows the stress variation around the riser circumference in the case of the current speed 0.44m/s. The maximum stress variation happened at the location corresponding to the cross-flow direction, at β=90 and 270 degree. Therefore, the following analysis focuses on the stress variation at β=90 degree.

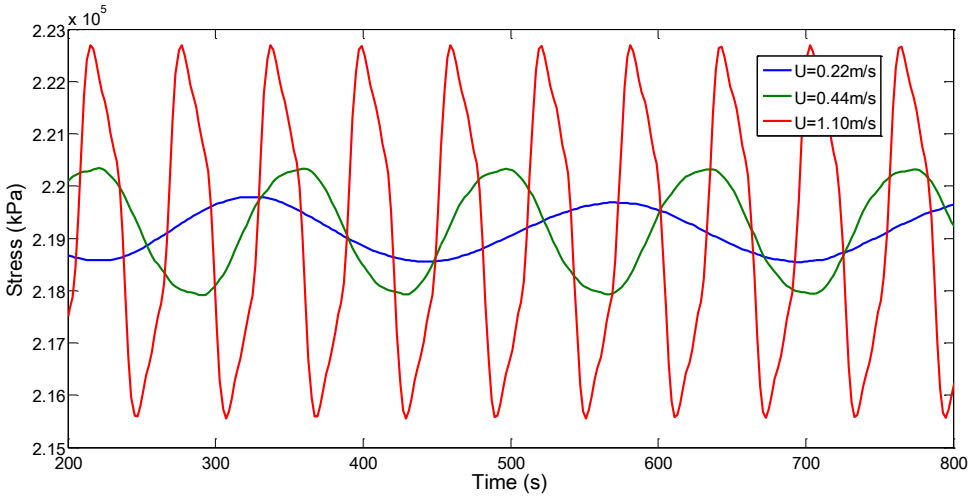

Figure 4.43 Stress variation under different current speeds

Figure 4.43 shows the time series of the stress at the vertical riser top end at β=90 degree. The frequency of the stress variation is the same as the vortex shedding frequency.

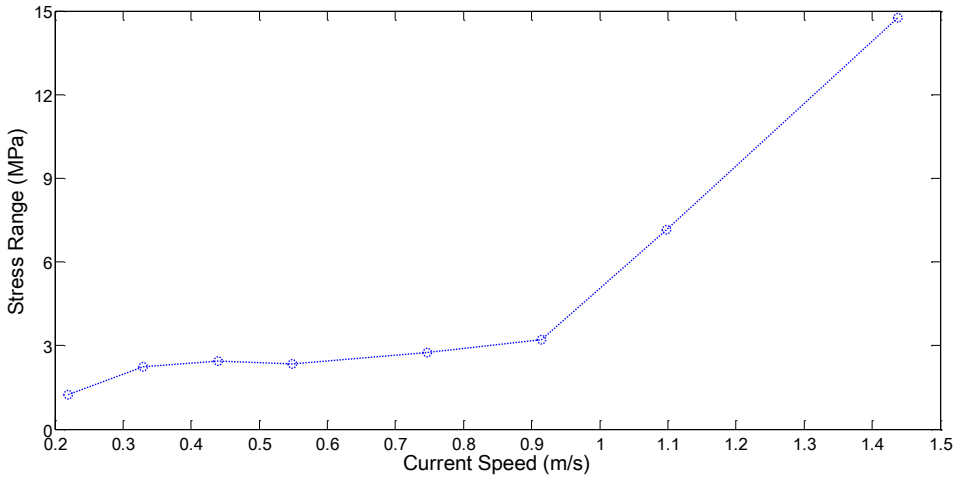

Figure 4.44 Stress range versus current speed

Figure 4.44 shows the stress variation for different current speeds. The stress variation increases with the increase in the current speed even when the buoyancy can oscillation amplitude decreases.

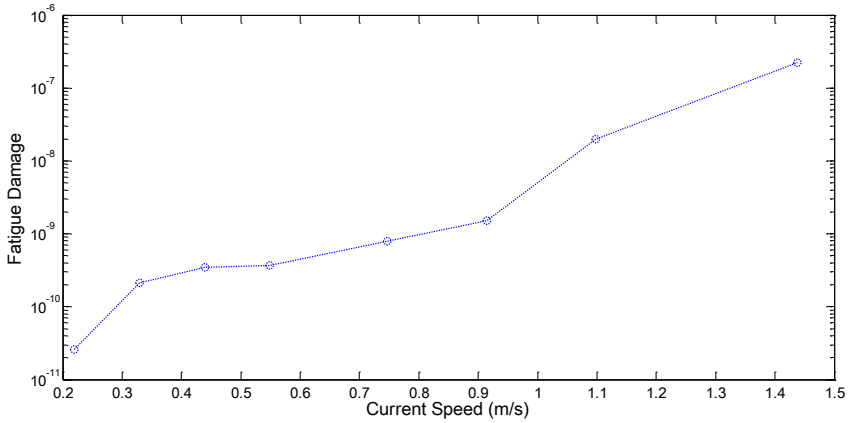

Figure 4.45 Fatigue damage at vertical riser top in 3 hours

Figure 4.45 shows the fatigue damage on the vertical riser top under different current speeds. The current speed is assumed to be constant in 3 hours. The buoyancy can VIM induced fatigue damage increases dramatically with the current speed.

4.4 Dynamic Simulations of the FSHR due to Combined Excitation

In this section, we consider the excitation of the FSHR system caused by both the vessel motion and the VIM of the buoyancy can. The current speed is assumed to be a constant at 0.44m/s. The vessel surge motion is sinusoidal with amplitude 30m and period 150s, and its heave motion is sinusoidal as well with amplitude 2m and period 15s. The following analysis is only performed for the FSHR of Case I.

4.4.1 Motion of the Upper Riser Assembly

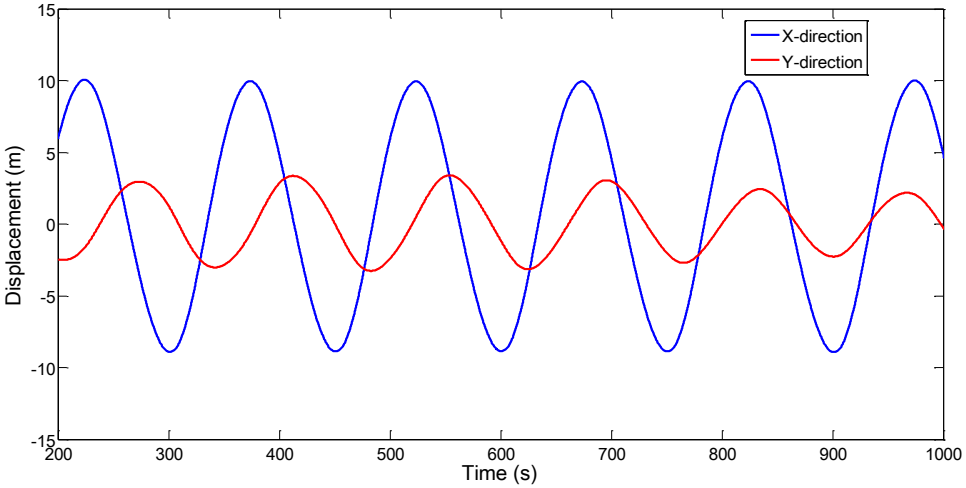

Figure 4.46 Motion of the URA

Figure 4.46 shows the time series of the motion of the URA in X and Y-direction. The period of motion in X-direction is the same as the period of the vessel surge motion at 150s. The period of motion of the URA in Y-direction is equal to the period of the VIM at 138s.

4.4.2 Stress on Vertical Riser Top End

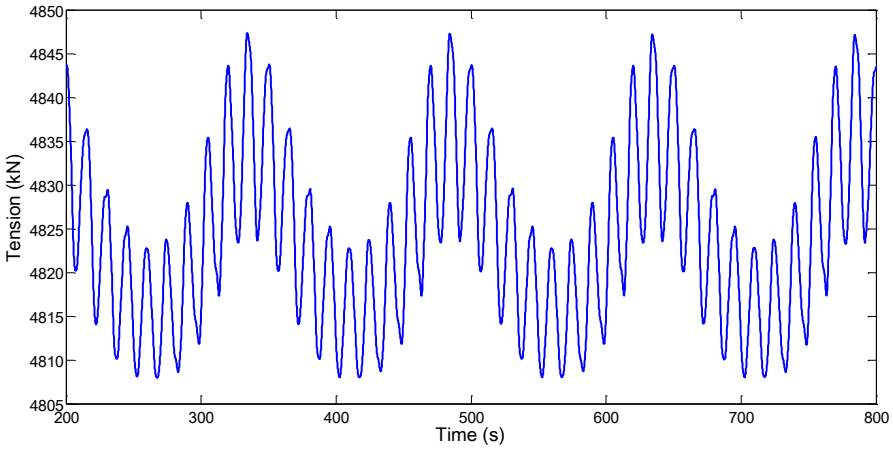

Figure 4.47 Tension at the vertical riser top end under combined excitations

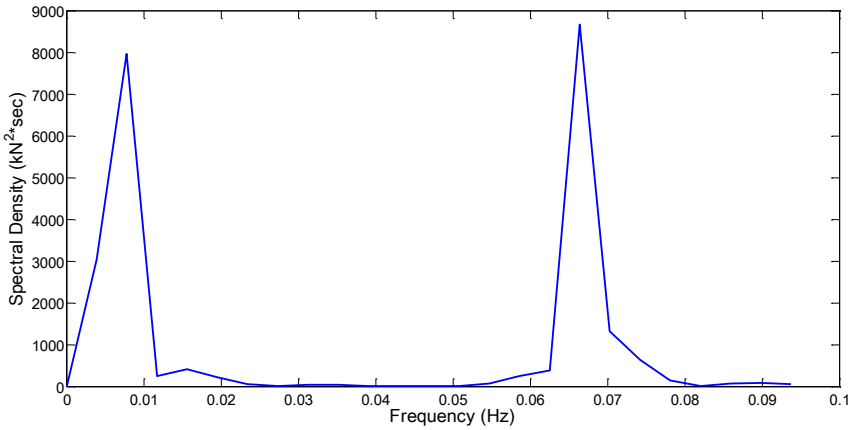

Figure 4.48 Spectrum of tension at the vertical riser top end

Figure 4.47 shows the time series of the top tension of the vertical riser and Figure 4.48 is the spectrum of the corresponding time series. The spectrum has two peak periods. The first peak period is 150s, which is the vessel surge motion period. The second peak period is 15s, the vessel heave motion period. The top tension of the vertical

riser is dominated by the vessel motion. The difference between the maximum and minimum value is only 0.82% of the mean top tension.

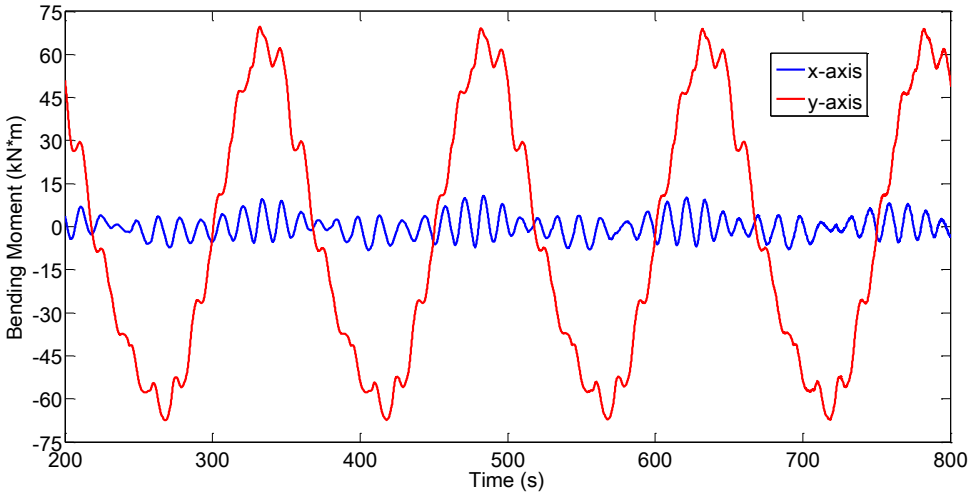

Figure 4.49 Bending moment at the vertical riser top end in x and y-axis

Figure 4.49 shows the time series of the bending moments with respect to the x and y-axis at the top of the riser (the x- and y-axis are defined in Figure 4.24). The bending moment with respect to x-axis is mainly induced by the buoyancy can VIM (cross-flow motion). The bending moment with respect to y-axis is mainly induced by the vessel motion (in-line motion). The bending moment variation with respect to y-axis has greater amplitude and period than those with respect to x-axis.

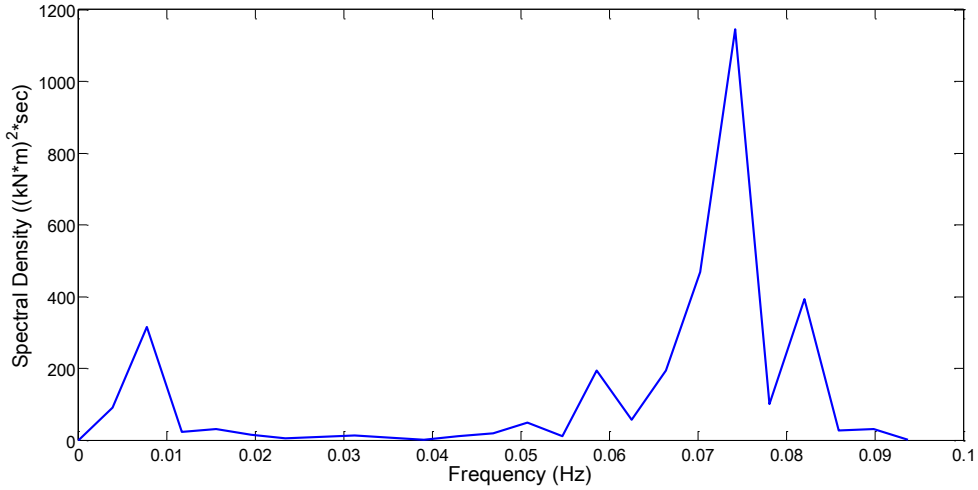

Figure 4.50 Spectrum of bending moment with respect to x-axis

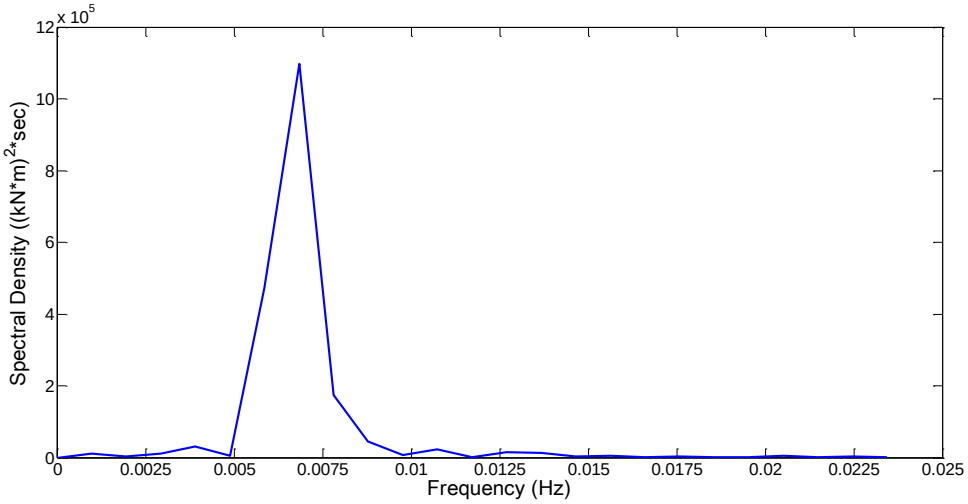

Figure 4.51 Spectrum of bending moment with respect to y-axis

Figure 4.50 and Figure 4.51 present the spectra of the bending moment with respect to x and y-axis, respectively. For the bending moment with respect to x-axis, four main peaks are observed. The peak periods are 138s, 17s, 13.47s and 12.2s. The dominant peak is at 13.47s, which is close to the vessel heave motion period 15s. The period of this dominant mode is much smaller than the motion of URA in cross-flow

direction, of which the period is 138s. Therefore, the combined excitation of the buoyancy can VIM and vessel heave motion can induce both the vortex shedding frequency response and the wave frequency response to the bending moment with respect to x-axis.

For the bending moment with respect to y-axis, the only peak period is 150s, which is the same as the vessel surge motion period (150s).

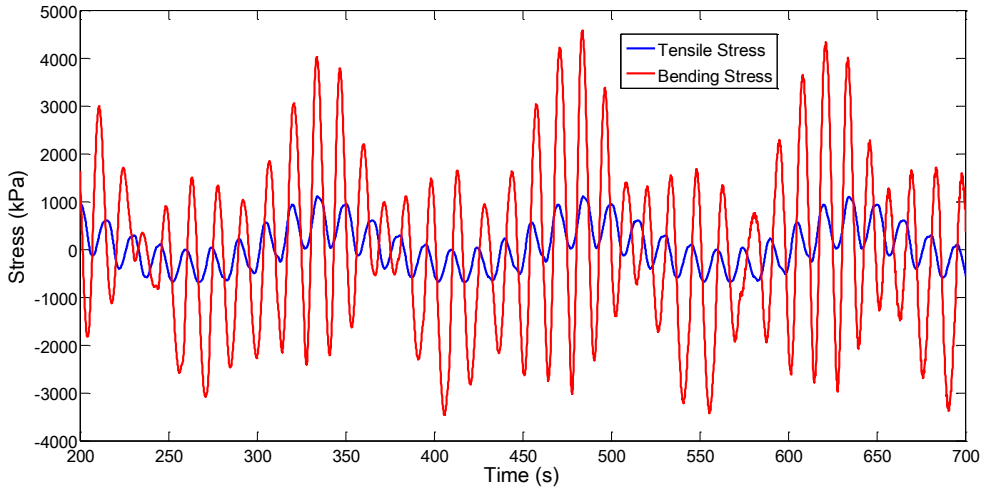

Figure 4.52 Tensile and bending stress at β=90 degree

Figure 4.52 shows time series of the tensile and bending stress at the location, β=90 degree. The stress variation is dominated by the variation in the bending stress.

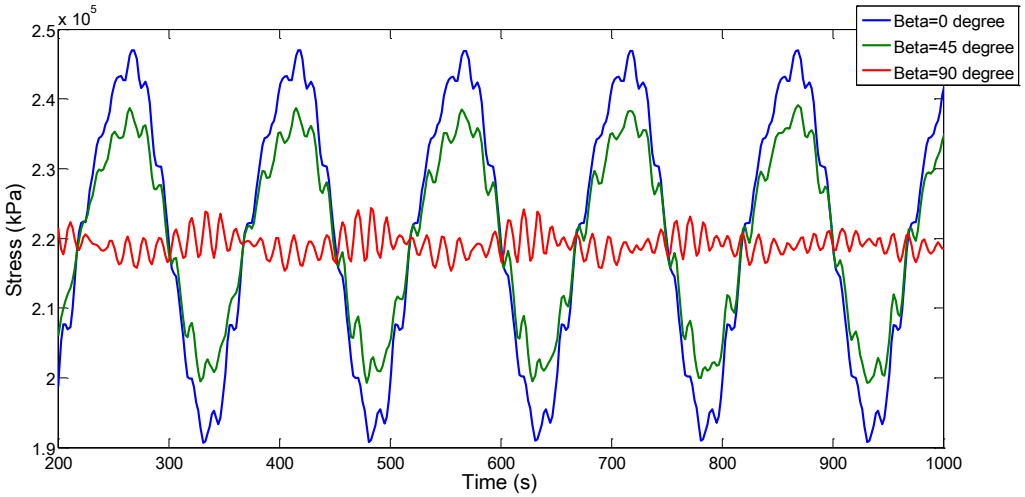

Figure 4.53 Stress at the vertical riser top end under combined excitations

Figure 4.53 shows the stress time series at the top of the riser of β=0, 45 and 90 degree, respectively. The stress variation at each β is dominated by the corresponding bending moment. Using the rainflow-counting algorithm and based on the S-N curve, the fatigue damage index is estimated.

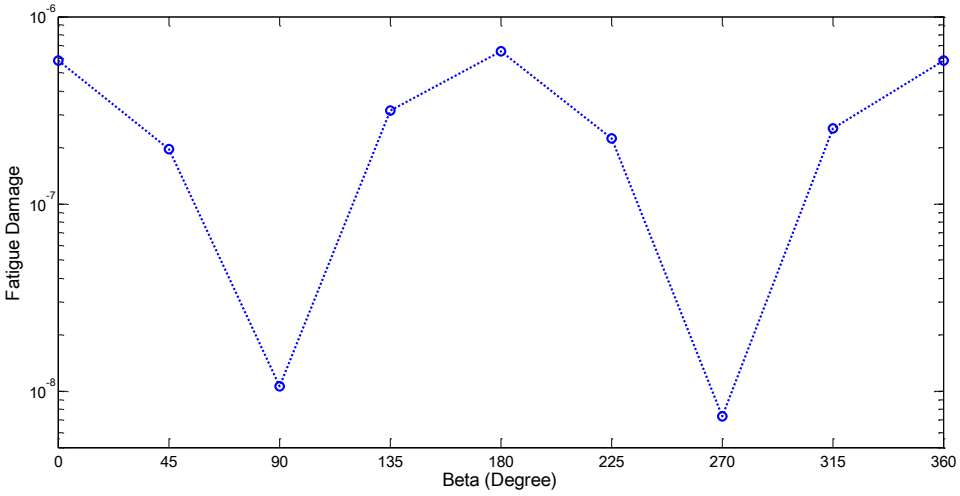

Figure 4.54 Fatigue damage in 3 hours

Figure 4.54 shows the fatigue damage index around the riser circumference caused by 3–hour excitation. It is assumed that the VIM of the buoyancy can and the vessel motion are steady within 3 hours. From the plot, the fatigue damage index at the in-line location (β=0 and 180 degree) is the greatest around the riser circumference, which is mainly caused by the vessel motion. However, fatigue damage index at β=90 and 270 degree caused by the VIM of the buoyancy can is comparable to the in-line fatigue damage index. The cross-flow fatigue damage index caused by the combined excitation of vessel motion and buoyancy can VIM is higher than fatigue index induced by buoyancy VIM only. Therefore, when calculating the cross-flow fatigue damage, it is recommended to perform the numerical simulation of the FSHR under the combined excitation of vessel motion and buoyancy can VIM simultaneously.

5. SUMMARY AND CONCLUSION

This study extends the existing in-house code, COUPLE, to allow for the numerical simulation of a Free Standing Hybrid Riser. A FSHR mainly consists of an upper riser assembly (URA), vertical riser, flexible jumper, buoyancy can and tether chain. In using COUPLE, the URA is modeled as a main body which is rigid and connects all the other components directly or indirectly. At its upper end, the vertical riser connects the URA through a clamped connector and at the lower end connects seabed pipe through a rotational spring. The buoyancy can connects the URA through a tether chain, providing the up-lifting tension to the URA and in turn to the vertical riser. The connectors of the chain to both buoyancy can and the URA are modeled as hinges. The flexible jumper transports oil or gas from the URA to a surface floater and the related connectors are modeled as clamped connectors. The numerical models for these boundary constraints applied on the vertical riser and jumper, namely rotational spring and clamped connector, are developed in this study for the simulation. The governing equations for the dynamics of the URA were solved numerically and coupled with those of the vertical riser, jumper and buoyancy can using COUPLE. Dynamic responses of the FSHR due to the motions of the floater are investigated in two cases of FSHRs deployed in different deep water depths. The numerical results are compared with the corresponding ones obtained using OrcaFlex, a commercial code widely used by the offshore industry. The comparison is found to be in satisfactory agreement. In addition, our simulation is also made for the VIM of the buoyancy can due to the presence of the

currents and in turn its effects on the motion of the URA and bending moments at the top of the vertical riser for the FSHR of Case I. It should be noted the type of simulation is not available in OrcaFlex yet. The following conclusions are drawn based on the simulated results.

1. When a FSHR is excited by the motion of a surface vessel, the oscillation of the URA and vertical riser is small in amplitude in comparison with that of the vessel. This is expected because they are connected by a flexible jumper, which effectively decouples the motion of the URA from the vessel motion.

2. Both tension and bending moment variations at the top end of the vertical riser resulting from the oscillation of the vessel are small. Therefore, the stress variation mainly contributed from the bending moment variation at the top of the vertical riser is small. Consequently the estimated fatigue damage index of the FSHR under the West of Africa Metocean condition is found out to be extremely small. This confirms the advantage of the use of a FSHR.

3. Based on the measured vortex shedding frequency and lifting force coefficient, it is shown that the VIM of the buoyancy can predicted using COUPLE closely matches that of the model test. The fatigue damage induced by the VIM of the buoyancy can increases significantly in the presence of currents.

4. In considering the combined excitation to the URA from both vessel‟s motion and buoyancy can VIM, the in-line motion of the URA mainly depends on the vessel‟s surge motion and the cross-flow motion is mainly on the VIM of the buoyancy can. In

general, the fatigue damage induced by the vessel‟s motion is greater than that induced by buoyancy can VIM.

REFERENCES

API Recommended Practice 2RD (API RP 2RD), 2006. Design of Risers for Floating Production Systems (FPSs) and Tension-Leg Platforms (TLPs). American Petroleum Institute, Washington, DC.

Bai, Y., and Bai, Q., 2005. Subsea Pipelines and Risers. Elsevier, Kidlington, Oxford, UK.

Chang, G., Tan, P., Huang, K. and Kwan, T., 2012, Effect of Polyester Mooring Stiffness on SCR Design for FPSO Application, International Conference on Ocean, Offshore and Arctic Engineering (OMAE), Rio de Janeiro, Brazil.

Chen, X.H., 2002, Studies on Dynamic Interaction between Deep-water Floating Structure and Their Mooring/Tendon Systems. PhD Dissertation, Texas A&M University, US.

Det Norske Veritas, Norway, 2010, DNV-RP-C203, Fatigue Design of Offshore Steel Structures.

Det Norske Veritas, Norway, 2010, DNV-RP-F205, Global Performance Analysis of Deepwater Floating Structures.

Garrett, D.L., 1982, Dynamic Analysis of Slender Rods. Journal of Energy Resources Technology, Transaction of ASME 104, 302-307.

Huang, H., 2013, Numerical Model of a Tensioner System and Flex Joint. Master Thesis, Texas A&M University, US.

Love, A.E.H., 1944. A Treatise on the Mathematical Theory of Elasticity. 4th Edition, Dover Publications, New York.

Ma, W., Webster, W.C., 1994. An Analytical Approach to Cable Dynamics: Theory and User Manual. SEA GRANT PROJECT R/OE-26.

Minguez, M., 2011, Slender Buoy VIM & VIR Analysis by CFD/FSI Approach, International Conference on Ocean, Offshore and Arctic Engineering (OMAE), Rotterdam, The Netherlands.

Morooka, C.K. and Shiguemoto D.A., 2006, Dynamics of a Vertical Riser with a Subsurface Buoy, International Conference on Ocean, Offshore and Arctic Engineering (OMAE), Rio de Janeiro, Brazil.

Nordgren, R.P., 1974. On Computation of the Motion of Elastic Rods. ASME Journal of Applied Mechanics, September, 777-780.

Paulling, J.R., Webster, W.C., 1986. A Consistent Large-amplitude Analysis of the Coupled Response of a TLP and Tendon System. Proceedings of Offshore Mechanics and Arctic Engineering (OMAE), Tokyo, Japan, Vol.3, pp. 126-133.

Pereira, P.S.D., Maeda, K., Morooka, C.K., Tamura, K., Itoh, K., 2005, Experimental Study on a Self Standing Hybrid Riser System throughout Tests on a Deep-Sea Model Basin, International Conference on Offshore Mechanics and Arctic Engineering (OMAE), Halkidiki, Greece.

Pereira, P.S.D., Morooka, C.K. and Champi, D.F., 2006, Dynamic Behavior Analysis of a Deepwater Self Standing Hybrid Riser System, International Society of Offshore and Polar Engineers (ISOPE), San Francisco, USA.

Roveri, F.E., Velten Filho, A.G., Mello, V.C., Marques, L.F., 2008, The Roncador P-52 Oil Export System – Hybrid Riser at 1800m Water Depth, Offshore Technology Conference (OTC), Houston, USA.

Song, R., Stanton, P., Zhou X., 2010, Engineering Design of Deepwater Free Standing Hybrid Riser, International Conference on Ocean, Offshore and Arctic Engineering (OMAE), Shanghai, China.

Wilde, J., 2007, Model Tests on the Vortex Induced Motions of the Air Can of A Free Standing Riser System in Current, Proc Deep Offshore Technology International Conference, Norway

APPENDIX I: MODELING ROTATIONAL SPRINGS

The flex joint behaves like and hence is modeled as a rotational spring. It is assumed that the moment exerted by a rotational spring on the riser is linearly proportional to the angle change between the tangential vector of the riser at the connection and the neutral axis of the rotational spring. However, the extension to allow for non-linear relation between the angle change and moment can be made with no principle difficulty.

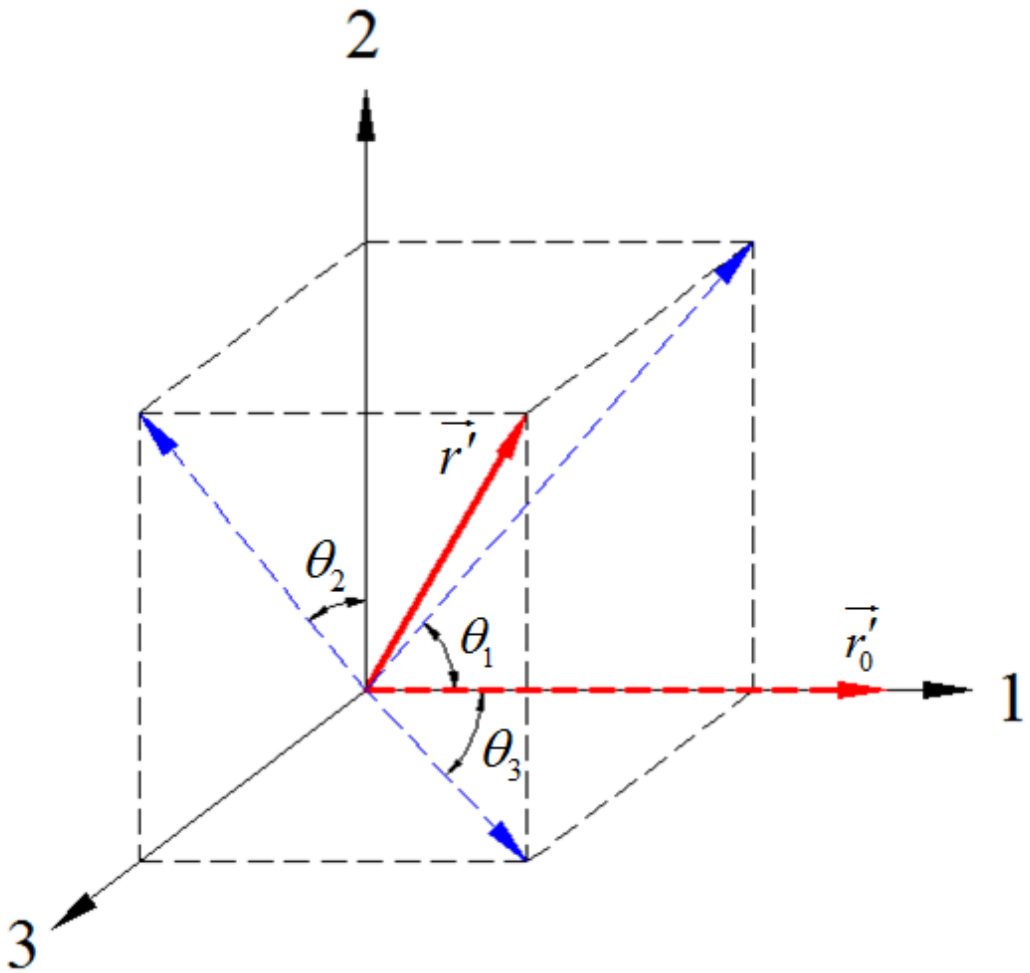

Figure I.1 Definitions for a Rotational Spring Model

The definitions used in modeling a rotational spring are sketched in Figure I.1. The red dashed line, $\vec{r}_0'$, is the neutral vector of a rotational spring, while solid red line, $\vec{r}'$, the tangential vector of the riser at time step, *t*. When the tangential vector of the riser is coincident with the neutral vector of the rotational spring, the moment applied by a rotational spring on the riser is equal to zero. Figure I.1 indicates that the coordinates 1-2-3 are fixed at the rotational spring with its neutral axis at the positive direction of the axis 1. The dashed blue lines are the projection of $\vec{r}'$ onto three planes of the coordinates, respectively. Therefore, the moment exerted on the riser by the rotational spring is given in equation (I1.1), where M_{0i} is the stiffness of a rotational spring in i-direction and i = 1 - 3.

$$\begin{aligned} \vec{M} &= (M_1, M_2, M_3) \\ M_1 &= M_{01}\theta_2 \\ M_2 &= M_{02}\theta_3 \\ M_3 &= M_{03}\theta_1 \end{aligned} \tag{II.1}$$

In COUPLE, the global system of equations, [A][δX]=[B], are solved for the increment in displacement. To account for the constraints of a rotational spring, the matrix and column vector, [A] and [B], are modified following the relationship between $\delta\theta$ and $\delta r_i'$.

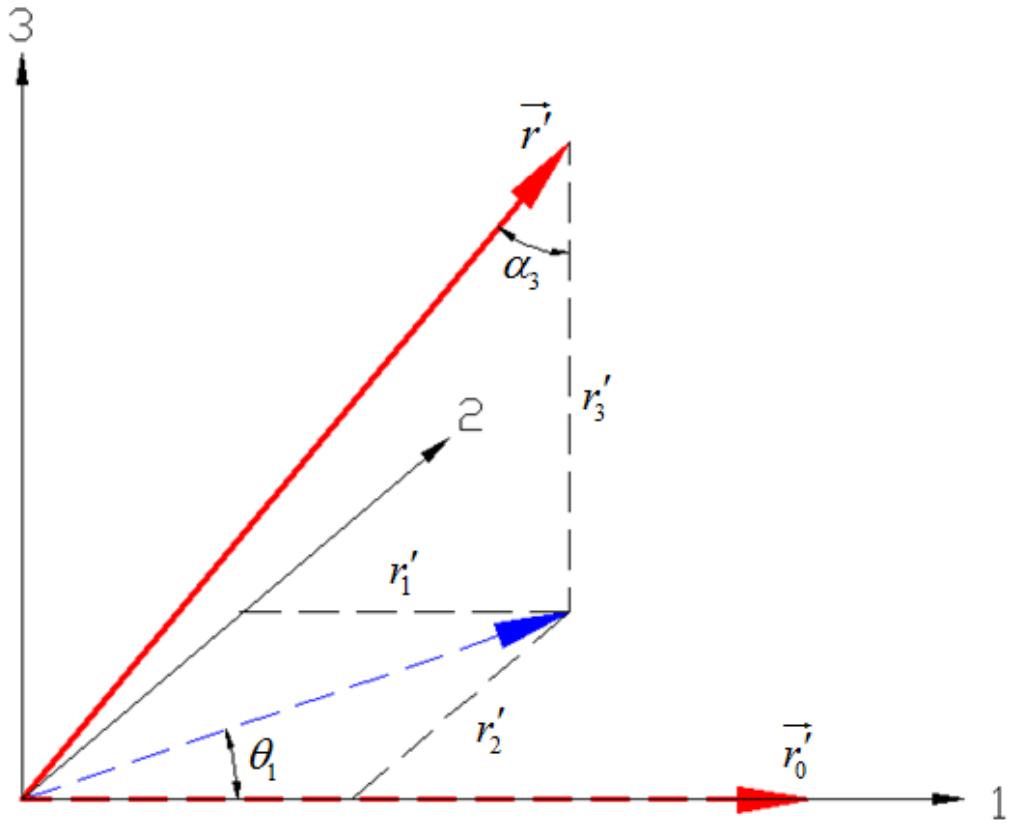

Figure I.2 Geometry Relationship

The three components of the tangential vector of the riser in the coordinates 1-2-3 are shown in Figure I.2. The following derivation is made to relate the increment in θ_1 to those in r_2' and r_3'.

$$r_2' = \left|\vec{r'}\right| \sin\alpha_3 \sin\theta_1 \tag{I.2}$$

$$\begin{aligned} r_2' + \delta r_2' &= \left|\vec{r'}\right| \sin(\alpha_3 + \delta\alpha_3)\cdot\sin(\theta_1 + \delta\theta_1) \\ &= \left|\vec{r'}\right| \left[\sin\alpha_3\cos\delta\alpha_3 + \cos\alpha_3\sin\delta\alpha_3\right]\cdot\left[\sin\theta_1\cos\delta\theta_1 + \cos\theta_1\sin\delta\theta_1\right] \\ &= \left|\vec{r'}\right| \left[\sin\alpha_3\sin\theta_1 + \sin\alpha_3\cos\theta_1\cdot\delta\theta_1 + \cos\alpha_3\sin\theta_1\cdot\delta\alpha_3\right] \end{aligned} \tag{I.3}$$

As $\delta\alpha_3, \delta\theta_1$ is small, $\cos\delta\alpha_3 \approx 1$, $\sin\delta\alpha_3 \approx \delta\alpha_3$, $\cos\delta\theta_3 \approx 1$, $\sin\delta\theta_3 \approx \delta\theta_3$. In the above approximation, the nonlinear terms related to small changes in α_3 and θ_1 are neglected. Comparing (I.2) with (I.3), equation (I.4) is derived.

$$\delta r_2' = \left|\vec{r'}\right| \left[\sin\alpha_3 \cos\theta_1 \cdot \delta\theta_1 + \cos\alpha_3 \sin\theta_1 \cdot \delta\alpha_3\right] \tag{I.4}$$

With similar approximations, we may derive the relationship between $\delta\alpha_3$ and $\delta r_3'$:

$$\begin{aligned} & r_3' = \left|\vec{r'}\right| \cos\alpha_3 \\ & r_3' + \delta r_3' = \left|\vec{r'}\right| \cos(\alpha_3 + \delta\alpha_3) = \left|\vec{r'}\right| (\cos\alpha_3 - \sin\alpha_3 \cdot \delta\alpha_3) \\ & \delta r_3' = -\left|\vec{r'}\right| \sin\alpha_3 \cdot \delta\alpha_3 \Rightarrow \delta\alpha_3 = \frac{-\delta r_3'}{\left|\vec{r'}\right| \sin\alpha_3} \end{aligned} \tag{I.5}$$

Substituting (I.5) into (I.4), $\delta\theta_1$ can be described by the increments in the tangential vector of the riser at the connection, $\delta r_2'$ and $\delta r_3'$.

$$\begin{aligned} & \delta r_2' = \left|\vec{r'}\right| \left[\sin\alpha_3 \cos\theta_1 \cdot \delta\theta_1 - \cos\alpha_3 \sin\theta_1 \cdot \frac{\delta r_3'}{\left|\vec{r'}\right| \sin\alpha_3}\right] \\ & \delta\theta_1 = \frac{\delta r_2' + \sin\theta_1 \cot\alpha_3 \cdot \delta r_3'}{\left|\vec{r'}\right| \sin\alpha_3 \cos\theta_1} \\ & \sin\theta_1 = \frac{r_2'}{\sqrt{\left|\vec{r'}\right|^2 - (r_3')^2}}, \quad \cot\alpha_3 = \frac{r_3'}{\sqrt{\left|\vec{r'}\right|^2 - (r_3')^2}}, \quad r_1' = \left|\vec{r'}\right| \sin\alpha_3 \cos\theta_1 \\ & \delta\theta_1 = \frac{\delta r_2' + \dfrac{r_2' \cdot r_3'}{\left|\vec{r'}\right|^2 - (r_3')^2} \cdot \delta r_3'}{r_1'} \end{aligned} \tag{I.6}$$

$$M_3 = M_{03}(\theta_1 + \delta\theta_1)$$
$$= M_{03}\left[\arcsin\left(\frac{r_2'}{\sqrt{\left|\vec{r'}\right|^2 - (r_3')^2}}\right) + \frac{\delta r_2' + \frac{r_2' \cdot r_3'}{\left|\vec{r'}\right|^2 - (r_3')^2} \cdot \delta r_3'}{r_1'}\right] \tag{I.7}$$

Similarly, we may derive the following relations in other two directions.

$$M_2 = M_{02}(\theta_3 + \delta\theta_3)$$
$$= M_{02}\left[\arcsin\left(\frac{r_3'}{\sqrt{\left|\vec{r'}\right|^2 - (r_2')^2}}\right) + \frac{\delta r_3' + \frac{r_2' \cdot r_3'}{\left|\vec{r'}\right|^2 - (r_2')^2} \cdot \delta r_2'}{r_1'}\right] \tag{I.8}$$

$$M_1 = M_{01}(\theta_2 + \delta\theta_2)$$
$$= M_{01}\left[\arcsin\left(\frac{r_3'}{\sqrt{\left|\vec{r'}\right|^2 - (r_1')^2}}\right) + \frac{\delta r_3' + \frac{r_1' \cdot r_3'}{\left|\vec{r'}\right|^2 - (r_1')^2} \cdot \delta r_1'}{r_2'}\right] \tag{I.9}$$

After Galerkin Method is used to get a series of ordinary differential equations, the right-hand-side terms are called generalized forces $\mathbf{f}_i$, and in particular the moment is given below,

$$\mathbf{f}_2 = -\frac{1}{L} B\mathbf{r}''(0) = \frac{1}{L}(\boldsymbol{r}' + \delta\boldsymbol{r}') \times \widetilde{\mathbf{M}}(0) \tag{I.10}$$

At the upper end of a vertical riser, in terms of the first element, $\mathbf{f}_2$ represents the moment, which is exerted by a rotational spring. Substituting the expression for $\boldsymbol{r}' + \delta\boldsymbol{r}'$ and (M_x, M_y, M_z), the expressions for f_{21}, f_{22}, f_{22} can be obtained. Adding this boundary

condition to the global system of equations, [A][δX]=[B], the effects of a rotational spring is included in the global equation.

$$\begin{aligned}\overrightarrow{f_2} &= \overrightarrow{r'(0)} \times \overrightarrow{M(0)} \\ &= \begin{vmatrix} \vec{i} & \vec{j} & \vec{k} \\ r_x' + \delta r_x' & r_y' + \delta r_y' & r_z' + \delta r_z' \\ M_x & M_y & M_z \end{vmatrix}\end{aligned} \tag{I.11}$$

$$\begin{bmatrix} n_{x1} & n_{x2} & n_{x3} \\ n_{y1} & n_{y2} & n_{y3} \\ n_{z1} & n_{z2} & n_{z3} \end{bmatrix} \begin{bmatrix} M_1 \\ M_2 \\ M_3 \end{bmatrix} = \begin{bmatrix} M_x \\ M_y \\ M_z \end{bmatrix} \tag{I.12}$$

In equation (I.12), (M_x, M_y, M_z) is the bending moment expressed in the global coordinate system of the riser, and (M_1, M_2, M_3) is the bending moment expressed in the body-fixed coordinate system of which the 1-axis is the neutral axis of the related rotational spring. [n] is the transfer matrix between these two coordinate systems.

Let

$$C_1 = \frac{r_1' \cdot r_3'}{(r_2')^2 + (r_3')^2}, \quad C_2 = \frac{r_2' \cdot r_3'}{(r_3')^2 + (r_1')^2}, \quad C_3 = \frac{r_2' \cdot r_3'}{(r_1')^2 + (r_2')^2}$$

$$\theta_1 = \arcsin\left(\frac{r_2'}{\sqrt{(r_1')^2 + (r_2')^2}}\right)$$

$$\theta_2 = \arcsin\left(\frac{r_3'}{\sqrt{(r_2')^2 + (r_3')^2}}\right)$$

$$\theta_3 = \arcsin\left(\frac{r_3'}{\sqrt{(r_3')^2 + (r_1')^2}}\right)$$

$$f_{21} = (r_y' + \delta r_y')M_z - (r_z' + \delta r_z')M_y$$

$$
\begin{aligned}
&(r_y' + \delta r_y')M_z \\
&= (r_y' + \delta r_y')\begin{Bmatrix} n_{z1}M_{01}(\theta_2 + \dfrac{\delta r_3' + C_1 \cdot \delta r_1'}{r_2'}) + \\ n_{z2}M_{02}(\theta_3 + \dfrac{\delta r_3' + C_2 \cdot \delta r_2'}{r_1'}) + \\ n_{z3}M_{03}(\theta_1 + \dfrac{\delta r_2' + C_3 \cdot \delta r_3'}{r_1'}) \end{Bmatrix} \\
&= r_y' \cdot \begin{Bmatrix} n_{z1}M_{01}\theta_2 + \\ n_{z2}M_{02}\theta_3 + \\ n_{z3}M_{03}\theta_1 \end{Bmatrix} + \delta r_y' \cdot \begin{Bmatrix} n_{z1}M_{01}\theta_2 + \\ n_{z2}M_{02}\theta_3 + \\ n_{z3}M_{03}\theta_1 \end{Bmatrix} + \\
&\quad r_y' \begin{Bmatrix} \dfrac{n_{z1}M_{01}}{r_2'}\left[(n_{x3} + C_1 n_{x1})\delta r_x' + (n_{y3} + C_1 n_{y1})\delta r_y' + (n_{z3} + C_1 n_{z1})\delta r_z'\right] + \\ \dfrac{n_{z2}M_{02}}{r_1'}\left[(n_{x3} + C_2 n_{x2})\delta r_x' + (n_{y3} + C_2 n_{y2})\delta r_y' + (n_{z3} + C_2 n_{z2})\delta r_z'\right] + \\ \dfrac{n_{z3}M_{03}}{r_1'}\left[(n_{x2} + C_3 n_{x3})\delta r_x' + (n_{y2} + C_3 n_{y3})\delta r_y' + (n_{z2} + C_3 n_{z3})\delta r_z'\right] \end{Bmatrix} \\
&(r_z' + \delta r_z')M_y \\
&= r_z' \cdot \begin{Bmatrix} n_{y1}M_{01}\theta_2 + \\ n_{y2}M_{02}\theta_3 + \\ n_{y3}M_{03}\theta_1 \end{Bmatrix} + \delta r_z' \cdot \begin{Bmatrix} n_{y1}M_{01}\theta_2 + \\ n_{y2}M_{02}\theta_3 + \\ n_{y3}M_{03}\theta_1 \end{Bmatrix} + \\
&\quad r_z' \begin{Bmatrix} \dfrac{n_{y1}M_{01}}{r_2'}\left[(n_{x3} + C_1 n_{x1})\delta r_x' + (n_{y3} + C_1 n_{y1})\delta r_y' + (n_{z3} + C_1 n_{z1})\delta r_z'\right] + \\ \dfrac{n_{y2}M_{02}}{r_1'}\left[(n_{x3} + C_2 n_{x2})\delta r_x' + (n_{y3} + C_2 n_{y2})\delta r_y' + (n_{z3} + C_2 n_{z2})\delta r_z'\right] + \\ \dfrac{n_{y3}M_{03}}{r_1'}\left[(n_{x2} + C_3 n_{x3})\delta r_x' + (n_{y2} + C_3 n_{y3})\delta r_y' + (n_{z2} + C_3 n_{z3})\delta r_z'\right] \end{Bmatrix}
\end{aligned}
$$

For short writing, we let

$$\begin{pmatrix} yz(1) = r_y' \cdot n_{z1} - r_z' \cdot n_{y1}, \\ yz(2) = r_y' \cdot n_{z2} - r_z' \cdot n_{y2}, \\ yz(3) = r_y' \cdot n_{z3} - r_z' \cdot n_{y3} \end{pmatrix}$$

$$\begin{aligned} f_{21} = & \begin{Bmatrix} yz(1)M_{01}\theta_2 + \\ yz(2)M_{02}\theta_3 + \\ yz(3)M_{03}\theta_1 \end{Bmatrix} + \begin{Bmatrix} yz(1)M_{01}\dfrac{n_{x3} + C_1 n_{x1}}{r_2'} + \\ yz(2)M_{02}\dfrac{n_{x3} + C_2 n_{x2}}{r_1'} + \\ yz(3)M_{03}\dfrac{n_{x2} + C_3 n_{x3}}{r_1'} \end{Bmatrix} \cdot \delta r_x' \\ & + \left\{ \begin{bmatrix} yz(1)M_{01}\dfrac{n_{y3} + C_1 n_{y1}}{r_2'} + \\ yz(2)M_{02}\dfrac{n_{y3} + C_2 n_{y2}}{r_1'} + \\ yz(3)M_{03}\dfrac{n_{y2} + C_3 n_{y3}}{r_1'} \end{bmatrix} + \begin{bmatrix} n_{z1}M_{01}\theta_2 + \\ n_{z2}M_{02}\theta_3 + \\ n_{z3}M_{03}\theta_1 \end{bmatrix} \right\} \cdot \delta r_y' \\ & + \left\{ \begin{bmatrix} yz(1)M_{01}\dfrac{n_{z3} + C_1 n_{z1}}{r_2'} + \\ yz(2)M_{02}\dfrac{n_{z3} + C_2 n_{z2}}{r_1'} + \\ yz(3)M_{03}\dfrac{n_{z2} + C_3 n_{z3}}{r_1'} \end{bmatrix} - \begin{bmatrix} n_{y1}M_{01}\theta_2 + \\ n_{y2}M_{02}\theta_3 + \\ n_{y3}M_{03}\theta_1 \end{bmatrix} \right\} \cdot \delta r_z' \end{aligned} \tag{I.13}$$

At right-hand-side of (I.13), the first term is the bending moment applied on the riser in the previous position, which is at the RHS of the global equation of the riser. The rest terms are the coefficients for the increment of the tangential vector at the first element of the riser. They are at the LHS of the global equation.

Similarly, we have the expressions for f_{22} and f_{23}.

$$
\begin{aligned}
f_{22} = & \begin{Bmatrix} zx(1)M_{01}\theta_2 + \\ zx(2)M_{02}\theta_3 + \\ zx(3)M_{03}\theta_1 \end{Bmatrix} + \left\{ \begin{bmatrix} zx(1)M_{01}\dfrac{n_{x3}+C_1 n_{x1}}{r_2'} + \\ zx(2)M_{02}\dfrac{n_{x3}+C_2 n_{x2}}{r_1'} + \\ zx(3)M_{03}\dfrac{n_{x2}+C_3 n_{x3}}{r_1'} \end{bmatrix} + \begin{bmatrix} n_{z1}M_{01}\theta_2 + \\ n_{z2}M_{02}\theta_3 + \\ n_{z3}M_{03}\theta_1 \end{bmatrix} \right\} \cdot \delta r_x', \\
& + \begin{bmatrix} zx(1)M_{01}\dfrac{n_{y3}+C_1 n_{y1}}{r_2'} + \\ zx(2)M_{02}\dfrac{n_{y3}+C_2 n_{y2}}{r_1'} + \\ zx(3)M_{03}\dfrac{n_{y2}+C_3 n_{y3}}{r_1'} \end{bmatrix} \cdot \delta r_y' \\
& + \left\{ \begin{bmatrix} zx(1)M_{01}\dfrac{n_{z3}+C_1 n_{z1}}{r_2'} + \\ zx(2)M_{02}\dfrac{n_{z3}+C_2 n_{z2}}{r_1'} + \\ zx(3)M_{03}\dfrac{n_{z2}+C_3 n_{z3}}{r_1'} \end{bmatrix} - \begin{bmatrix} n_{x1}M_{01}\theta_2 + \\ n_{x2}M_{02}\theta_3 + \\ n_{x3}M_{03}\theta_1 \end{bmatrix} \right\} \cdot \delta r_z'
\end{aligned} \tag{I.14}
$$

$$
\begin{pmatrix} zx(1) = r_z' \cdot n_{x1} - r_x' \cdot n_{z1}, \\ zx(2) = r_z' \cdot n_{x2} - r_x' \cdot n_{z2}, \\ zx(3) = r_z' \cdot n_{x3} - r_x' \cdot n_{z3} \end{pmatrix}
$$

$$
\begin{aligned}
f_{23} = & \begin{Bmatrix} xy(1)M_{01}\theta_2 + \\ xy(2)M_{02}\theta_3 + \\ xy(3)M_{03}\theta_1 \end{Bmatrix} + \left\{ \begin{bmatrix} xy(1)M_{01}\dfrac{n_{x3}+C_1 n_{x1}}{r_2'} + \\ xy(2)M_{02}\dfrac{n_{x3}+C_2 n_{x2}}{r_1'} + \\ xy(3)M_{03}\dfrac{n_{x2}+C_3 n_{x3}}{r_1'} \end{bmatrix} + \begin{bmatrix} n_{y1}M_{01}\theta_2 + \\ n_{y2}M_{02}\theta_3 + \\ n_{y3}M_{03}\theta_1 \end{bmatrix} \right\} \cdot \delta r_x', \\
& + \left\{ \begin{bmatrix} xy(1)M_{01}\dfrac{n_{y3}+C_1 n_{y1}}{r_2'} + \\ xy(2)M_{02}\dfrac{n_{y3}+C_2 n_{y2}}{r_1'} + \\ xy(3)M_{03}\dfrac{n_{y2}+C_3 n_{y3}}{r_1'} \end{bmatrix} - \begin{bmatrix} n_{x1}M_{01}\theta_2 + \\ n_{x2}M_{02}\theta_3 + \\ n_{x3}M_{03}\theta_1 \end{bmatrix} \right\} \cdot \delta r_y' \\
& + \begin{bmatrix} xy(1)M_{01}\dfrac{n_{z3}+C_1 n_{z1}}{r_2'} + \\ xy(2)M_{02}\dfrac{n_{z3}+C_2 n_{z2}}{r_1'} + \\ xy(3)M_{03}\dfrac{n_{z2}+C_3 n_{z3}}{r_1'} \end{bmatrix} \cdot \delta r_z'
\end{aligned} \tag{I.15}
$$

$$
\begin{pmatrix} xy(1) = r_x' \cdot n_{y1} - r_y' \cdot n_{x1}, \\ xy(2) = r_x' \cdot n_{y2} - r_y' \cdot n_{x2}, \\ xy(3) = r_x' \cdot n_{y3} - r_y' \cdot n_{x3} \end{pmatrix}
$$

The coefficients related to $\delta r_x'$, $\delta r_y'$, $\delta r_z'$ will be added to the LHS of the equation.

$$
\begin{bmatrix} f_{21} \\ f_{22} \\ f_{23} \end{bmatrix} = [\mathbf{a}] \begin{bmatrix} \delta r_x' \\ \delta r_y' \\ \delta r_z' \end{bmatrix} + [\mathbf{b}] \tag{I.16}
$$

APPENDIX II: MOTION RAO OF FPSO

The motion response amplitude operator (RAO) of the FPSO is used to determine the displacement of the flexible jumper at its hangout point as a function of time. The excitation to a FSHR provided by the flexible jumper which is connected to the FPSO under the impact of irregular waves is crucial to estimate the fatigue damage to a Free Standing Hybrid Riser. The wave direction used in the analysis is 0 degree with respect to the X-axis in the global coordinate system. Due to the symmetry of FPSO, the sway, roll and yaw RAO at the wave heading 0 degree are neglected. The surge, heave and pitch RAO are shown in the figures below, which are provided by Chang (2012). Knowing the peak period and significant wave height of irregular waves and the location of the hang-off point with respect to the center of gravity of the FPSO, the displacement of the hang-off point as a function can be calculated, which is used as the input for the simulation of the dynamics of a FSHR.

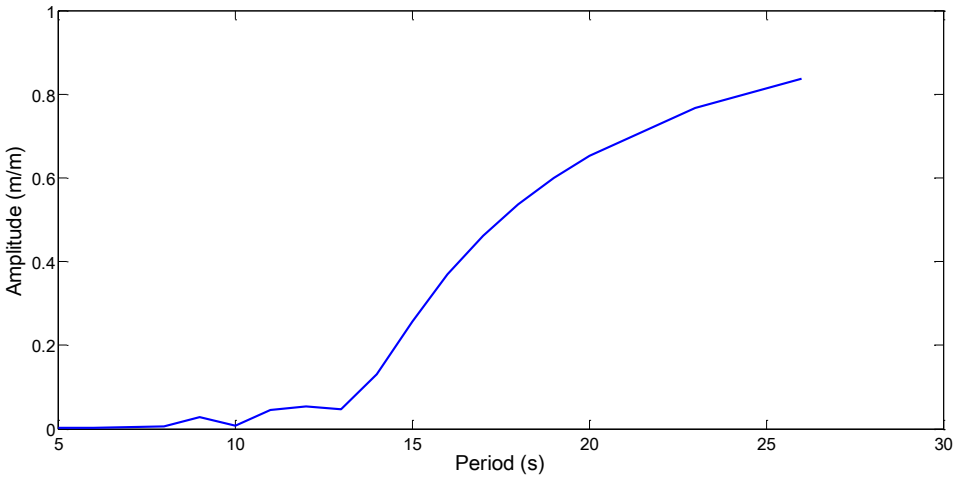

Figure II.1 Surge RAO

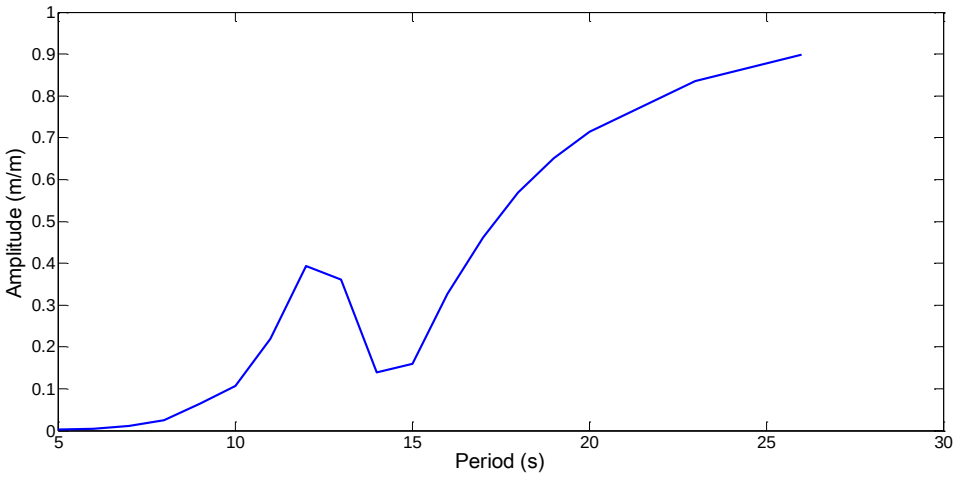

Figure II.2 Heave RAO

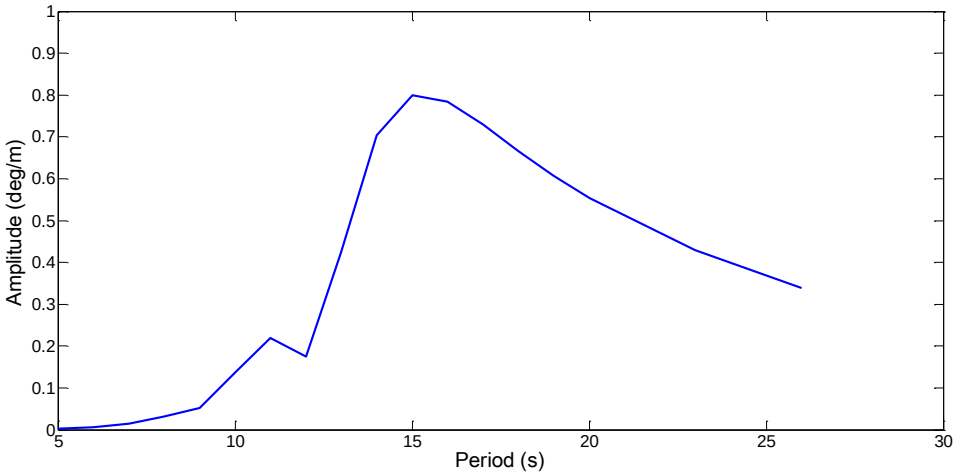

Figure II.3 Pitch RAO